Bound states in vortex cores of type-II superconductors

Numerical solution of the Bogoliubov-de Gennes equations on a disc

Bachelor thesis
Written by *Emil Jermiin Pedersen Frost*
June 16, 2021

Supervised by
Brian Møller Andersen

University of Copenhagen

UNIVERSITY OF COPENHAGEN

Faculty:	Faculty of Science
Department:	Niels Bohr Institute
Author:	Emil Jermiin Pedersen Frost
Email:	whj419@alumni.ku.dk
Title and subtitle:	Bound states in vortex cores of type-II superconductors - Numerical solution of the Bogoliubov-de Gennes equations on a disc
Supervisor:	Brian Møller Andersen
Handed in:	16.06.2021
Defended:	23.06.2021

Name ____________________

Signature ____________________

Date ____________________

Abstract

This thesis reproduces and expands on some of the theoretical work on *"Quantum Anomalous Vortex and Majorana Zero Mode in Iron-Based Superconductor Fe(Te,Se)"* by Jiang et al. [2] while showing good qualitative agreement with their results. We show that a magnetic impurity such as an interstitial Fe atom in Fe(Te,Se) may give rise to a spontaneously generated anomalous vortex (zero magnetic field) nucleated around the impurity in a superconductor with strong spin-orbit coupling or long-ranged exchange interaction. Additionally, we find that anti-ferromagnetic exchange interactions do not create favorable conditions for a vortex state in zero magnetic field while extended ferromagnetic islands, in some situations, do. Furthermore, we show the presence and isolation of a Majorana zero-energy mode in the helical Dirac fermion topological surface state (TSS) coupled to an impurity-induced anomalous vortex in a hole-like parabolic band of the bulk material. An external magnetic field is calculated to cause no energy shift of the Majorana mode but a noticeable shift in the energy of impurity-induced tuned zero-energy bound states of a vortex-free state in both the parabolic band and TSS that are not topologically protected.

Contents

1 Introduction

Many experiments have been conducted with the superconducting material Fe(Te,Se), exploring its remarkable properties. Some of these experiments probe the local density of states (LDOS) near excess Fe impurities, revealing a robust zero energy bound state (ZBS) present in zero external magnetic field with no energy shift when a strong magnetic field is applied – consistent with a Majorana zero-energy mode (MZM) [1]. The theoretical work by Jiang et al. [2] (referred to as 'QAV-paper' in the rest of the thesis) explains this by coupling a spontaneously generated anomalous vortex (no ext. magnetic field required) nucleated around interstitial Fe impurity sites in the bulk material to the topological surface states (TSS) of Fe(Te,Se), giving rise to the MZM. It has previously been shown that a helical Dirac fermion TSS contains a MZM [3]. Their analysis provides the starting ground for this thesis and presents logical opportunities for comparison. We will primarily be concerned with the requirements for the realization of an anomalous vortex. In doing so, we will both reproduce some of the results in the QAV-paper and explore both anti-ferromagnetic (AFM) and extended ferromagnetic (FM) exchange interactions. We will also show the presence of the MZM in the TSS and compare the Zeeman splitting to other possible impurity-induced ZBSs in vortex-free states.

2 Theory

The foundation of this theoretical study of anomalous vortices and zero-energy bound states in unconventional superconductors will be the model used in the QAV-paper which will be outlined accordingly. The central element is, of course, the Hamiltonian which we will try to diagonalize and in doing so, (re)discover the Bogoliubov-de Gennes equations that set the stage for the inevitable numerical work.

2.1 Theoretical model

We give here a somewhat brief description of the theoretical model used in the QAV-paper to model Fe(Te,Se) close to interstitial Fe impurities– see the article for details.

Consider a type-II s-wave superconductor with intrinsic spin-orbit coupling (SOC) in the limit $\lambda \gg \xi$, where λ is the penetration depth and ξ is the coherence length. We view the superconductor as a collection of stacked layers of 2-D superconducting material and treat the bulk material separately from the surface layer. Due to the close proximity of the surface layer, superconductivity is induced in it from the bulk material. We focus our attention on a single bulk layer with the 2-D geometry of a disc with radius R and conveniently express the points on the disc in polar coordinates $\boldsymbol{r} = (r, \theta)$. In the center at $r = 0$, a single magnetic impurity ion is embedded with magnetic moment $\boldsymbol{I}_{imp}$. This gives rise to the so-called Elliot-Yafet SOC and an exchange interaction between the impurity ion and the electrons in the metal. These effects imply that, close to the impurity, the superconducting state is non-uniform and the order parameter is spatially dependent even in the vortex-free case.

Superconductivity is, in itself, a many-body phenomenon which suggests the use of the second quantization formalism. We will study this problem with a real space representation of the Hamiltonian in terms of second quantization field operators. We denote the creation and annihilation field operators by $\Psi^\dagger_\sigma(\boldsymbol{r})$ and $\Psi_\sigma(\boldsymbol{r})$, respectively. They simply create or annihilate an electron at point $\boldsymbol{r}$ of spin $\sigma \in \{\uparrow, \downarrow\}$ and satisfy fermionic anti-commutation relations [4]:

$$\left\{\Psi_\sigma(\boldsymbol{r}), \Psi_{\sigma'}(\boldsymbol{r}')\right\} = \left\{\Psi^\dagger_\sigma(\boldsymbol{r}), \Psi^\dagger_{\sigma'}(\boldsymbol{r}')\right\} = 0, \; \left\{\Psi_\sigma(\boldsymbol{r}), \Psi^\dagger_{\sigma'}(\boldsymbol{r}')\right\} = \delta(\boldsymbol{r} - \boldsymbol{r}')\delta_{\sigma\sigma'}. \tag{2.1}$$

The first δ is the Dirac delta function while the last is a Kronecker delta; the spatial variable is continuous while spin is discrete.

In this theoretical model, we assume an effective Hamiltonian of the form:

$$H = \int \mathrm{d}\boldsymbol{r}\, \Psi^\dagger(\boldsymbol{r}) \hat{H}_N(\boldsymbol{r}) \Psi(\boldsymbol{r}) \; + \left[\Delta(\boldsymbol{r})\Psi^\dagger_\uparrow(\boldsymbol{r})\Psi^\dagger_\downarrow(\boldsymbol{r}) + \text{h.c.}\right], \tag{2.2}$$

expressed in spinor notation with $\Psi(\boldsymbol{r}) = (\Psi_\uparrow(\boldsymbol{r}), \Psi_\downarrow(\boldsymbol{r}))^T$ and $\Delta(\boldsymbol{r}) = -\frac{g}{2}\left\langle \Psi_\downarrow(\boldsymbol{r})\Psi_\uparrow(\boldsymbol{r})\right\rangle$ being the pair potential with g the attraction strength. We return to the pair potential in section 2.3. For the bulk states, the operator corresponding to the normal part of the Hamiltonian (normal in contrast to the pairing part in square brackets) is given by

$$\begin{gathered} \hat{H}_N = \hat{H}_{kin} + \hat{H}_{soc} + \hat{H}_{ex}, \\ \hat{H}_{kin} = -\frac{(\boldsymbol{p} - e\boldsymbol{A})^2}{2m^*} - \mu, \qquad \hat{H}_{soc} = -\lambda_{so}(r)\boldsymbol{L}\cdot\boldsymbol{\sigma}, \qquad \hat{H}_{ex} = -\mathcal{J}_{ex}(r)\boldsymbol{I}_{imp}\cdot\boldsymbol{J}, \end{gathered} \tag{2.3}$$

in the continuum limit. The kinetic part describes simple parabolic dispersion of a hole-like band with effective mass m^* and canonical momentum as is required by gauge invariance. The particle number is not conserved for this Hamiltonian if we look at the pairing part so we consider a grand canonical ensemble and assert that the system is in thermodynamic equilibrium with a large reservoir; this fixes the chemical potential μ and temperature T.

We will only consider the case of zero temperature where the chemical potential equals the Fermi energy ε_f.

$\hat{H}_{soc}$ is the Elliot-Yafet SOC which couples the orbital and spin angular momentum of the electrons. $\boldsymbol{L} = \boldsymbol{r} \times (\boldsymbol{p} - e\boldsymbol{A})$ is the orbital angular momentum operator while $\frac{\hbar}{2}\boldsymbol{\sigma}$ is the spin angular momentum operator with $\boldsymbol{\sigma} = (\sigma_x, \sigma_y, \sigma_z)$ being the Pauli matrices. The magnetic moment of the impurity couples to the total angular momentum $\boldsymbol{J} = \boldsymbol{L} + \frac{\hbar}{2}\boldsymbol{\sigma}$ of the electrons through the exchange interaction expressed in $\hat{H}_{ex}$ with exchange coupling $\mathcal{J}_{ex}(r)$. SOC and exchange interaction only affect the electrons in close proximity to the impurity ion. For simplicity, these two effects are assumed to be isotropic and, furthermore, described by the same spatial dependence: $\lambda_{so}(r), \mathcal{J}_{ex}(r) \propto e^{-r/r_0}$ with some characteristic decay length r_0. Moreover, we assume that the magnetic moment of the impurity ion is perpendicular to the superconducting 2-D layer, i.e. $\boldsymbol{I}_{imp} = M\hat{\boldsymbol{z}}$. We're restricting the particles to move in two dimensions only, such that $\boldsymbol{L} \cdot \boldsymbol{\sigma} = L_z\sigma_z$. Writing everything out for clarity, we assume $\hat{H}_N$ is given by

$$\hat{H}_N = -\frac{(\boldsymbol{p} - e\boldsymbol{A})^2}{2m^*} - \varepsilon_f - \lambda_{so}(r)L_z\sigma_z - m(r)\left(L_z + \frac{\hbar}{2}\sigma_z\right) \tag{2.4}$$

for the bulk states where $m(r) = \mathcal{J}_{ex}(r)M = m_0 e^{-r/r_0}$ and $\lambda_{so}(r) = \lambda_0 e^{-r/r_0}$.

For the surface layer in the vicinity of an impurity, we assume a so-called helical Dirac fermion topological surface state (TSS) for the kinetic part such that the effective Hamiltonian is of the form

$$\begin{gathered}\hat{H}'_N = \hat{H}'_{kin} + \hat{H}'_{soc} + \hat{H}'_{ex}, \\ \hat{H}'_{kin} = v_D\left(\boldsymbol{\sigma} \times (\boldsymbol{p} - e\boldsymbol{A})\right) \cdot \hat{\boldsymbol{z}} - \varepsilon'_f, \quad \hat{H}'_{soc} = \lambda'_{so}(r)L_z\sigma_z, \quad \hat{H}'_{ex} = -m'(r)J_z.\end{gathered} \tag{2.5}$$

We use primed variables for the TSS. In general, $\lambda'_{so}(r)$ and $m'(r)$ may be different from the unprimed variables in the bulk layers.

2.2 The Bogoliubov-de Gennes equations

With the Hamiltonian in place, the next step is to find a transformation that diagonalizes it. It's possible to do this with a Bogoliubov transformation. This is an expansion of the field operators in a set of fermionic operators $\gamma_n^\dagger, \gamma_n$ which have no spatial dependence themselves. These operators create or annihilate Bogoliubov quasiparticles - the low energy excitations of the superconductor.

$$\Psi_\sigma(\boldsymbol{r}) = \sum_n u_{n\sigma}(\boldsymbol{r})\gamma_n + v^*_{n\sigma}(\boldsymbol{r})\gamma_n^\dagger, \tag{2.6a}$$

$$\Psi_\sigma^\dagger(\boldsymbol{r}) = \sum_n u^*_{n\sigma}(\boldsymbol{r})\gamma_n^\dagger + v_{n\sigma}(\boldsymbol{r})\gamma_n. \tag{2.6b}$$

These particular linear combinations can be considered an *ansatz* which will be justified below. If the relations are inverted it becomes clear that the quasiparticles are superpositions of electron and hole states (see appendix A and eq. (A.1) in particular). The index n simply labels the states in whatever basis diagonalizes the Hamiltonian. The demand that the operators $\gamma_n^\dagger, \gamma_n$ are, in fact, fermionic is manifested in similar anti-commutation relations to eq. (2.1).

$$\{\gamma_n, \gamma_{n'}\} = \left\{\gamma_n^\dagger, \gamma_{n'}^\dagger\right\} = 0, \ \left\{\gamma_n, \gamma_{n'}^\dagger\right\} = \delta_{nn'}. \tag{2.7}$$

We postulate that this particular decomposition (2.6) will diagonalize the Hamiltonian (2.2) for some functions $u_{n\sigma}(\boldsymbol{r})$ and $v_{n\sigma}(\boldsymbol{r})$, i.e.

$$H = E_0 + \sum_n E_n \gamma_n^\dagger \gamma_n, \tag{2.8}$$

where E_0 is some constant and E_n is the energy spectrum of the Bogoliubov quasiparticles; both measured from the Fermi energy. The method we will use to diagonalize H won't give us E_0 but only the energy spectrum E_n. We will return to this point later when we need to calculate the total energy of the system. The combination $\gamma_n^\dagger\gamma_n$ in eq. (2.8) simply counts the number of particles in that state. In this diagonalized form, then, the energy of the thermal state $\langle H\rangle$ is just a sum of the energies of the occupied quasiparticle states (and the vacuum state energy). Since the particles are fermions, in thermal equilibrium, the average particle number is given by the Fermi-Dirac distribution. The following mean value rules apply [4]:

$$\langle \gamma_n \gamma_{n'}\rangle = \left\langle \gamma_n^\dagger \gamma_{n'}^\dagger \right\rangle = 0, \quad \left\langle \gamma_n^\dagger \gamma_{n'}\right\rangle = \delta_{nn'} n_F(E_n), \tag{2.9}$$

where $n_F(E_n) = [\exp(E_n/k_BT) + 1]^{-1}$ with k_B being Boltzmann's constant.

To determine the wave functions $u_{n\sigma}(\boldsymbol{r})$ and $v_{n\sigma}(\boldsymbol{r})$ that diagonalize the Hamiltonian, we evaluate the commutator $[\Psi_\sigma(\boldsymbol{r}), H]$ with both the original Hamiltonian (2.2) and the diagonalized form (2.8). We begin with the original Hamiltonian. It's helpful to use the identity $[A, BC] = \{A, B\}C - B\{A, C\}$ together with the fermionic anti-commutation relations from eq. (2.1). We consider the general case in which $\hat{H}_N$ is not diagonal which we need for the TSS. The following calculation is thus valid for both bulk and surface states. We label the entries in the 2×2 matrix $\hat{H}_N$ by $\hat{H}_N^{\alpha\beta}$.

$$
\begin{aligned}
[\Psi_\sigma(\boldsymbol{r}), H] &= \left[\Psi_\sigma(\boldsymbol{r}), \int \mathrm{d}\boldsymbol{r}' \sum_{\alpha\beta} \Psi_\alpha^\dagger(\boldsymbol{r}')\hat{H}_N^{\alpha\beta}(\boldsymbol{r}')\Psi_\beta(\boldsymbol{r}') + \left(\Delta(\boldsymbol{r}')\Psi_\uparrow^\dagger(\boldsymbol{r}')\Psi_\downarrow^\dagger(\boldsymbol{r}') + \text{h.c.}\right)\right], \\
&= \int \mathrm{d}\boldsymbol{r}' \sum_{\alpha\beta} \left\{\Psi_\sigma(\boldsymbol{r}), \Psi_\alpha^\dagger(\boldsymbol{r}')\right\}\hat{H}_N^{\alpha\beta}(\boldsymbol{r}')\Psi_\beta(\boldsymbol{r}') - \Psi_\alpha^\dagger(\boldsymbol{r}')\left\{\Psi_\sigma(\boldsymbol{r}), \hat{H}_N^{\alpha\beta}(\boldsymbol{r}')\Psi_\beta(\boldsymbol{r}')\right\}, \\
&\quad + \Delta(\boldsymbol{r}')\left(\left\{\Psi_\sigma(\boldsymbol{r}), \Psi_\uparrow^\dagger(\boldsymbol{r}')\right\}\Psi_\downarrow^\dagger(\boldsymbol{r}') - \Psi_\uparrow^\dagger(\boldsymbol{r}')\left\{\Psi_\sigma(\boldsymbol{r}), \Psi_\downarrow^\dagger(\boldsymbol{r}')\right\}\right), \\
&= \sum_\beta \hat{H}_N^{\sigma\beta}(\boldsymbol{r})\Psi_\beta(\boldsymbol{r}) + \Delta(\boldsymbol{r})\left(\delta_{\sigma\uparrow}\Psi_\downarrow^\dagger(\boldsymbol{r}) - \delta_{\sigma\downarrow}\Psi_\uparrow^\dagger(\boldsymbol{r})\right).
\end{aligned}
\tag{2.10}
$$

We can combine the cases for spin up and down in the following way:

$$
[\Psi(\boldsymbol{r}), H] = \begin{pmatrix} [\Psi_\uparrow(\boldsymbol{r}), H] \\ [\Psi_\downarrow(\boldsymbol{r}), H] \end{pmatrix} = \hat{H}_N(\boldsymbol{r})\Psi(\boldsymbol{r}) + \Delta(\boldsymbol{r}) i\sigma_y \left(\Psi^\dagger(\boldsymbol{r})\right)^T. \tag{2.11}
$$

Using the Bogoliubov transformation defined in eq. (2.6) we can express this result in terms of the quasiparticle operators $\gamma_n^\dagger, \gamma_n$.

$$
[\Psi(\boldsymbol{r}), H] = \sum_n \left[\hat{H}_N(\boldsymbol{r})\begin{pmatrix} u_{n\uparrow}(\boldsymbol{r}) & v_{n\uparrow}^*(\boldsymbol{r}) \\ u_{n\downarrow}(\boldsymbol{r}) & v_{n\downarrow}^*(\boldsymbol{r}) \end{pmatrix} + \Delta(\boldsymbol{r})\begin{pmatrix} v_{n\downarrow}(\boldsymbol{r}) & u_{n\downarrow}^*(\boldsymbol{r}) \\ -v_{n\uparrow}(\boldsymbol{r}) & -u_{n\uparrow}^*(\boldsymbol{r}) \end{pmatrix}\right]\begin{pmatrix} \gamma_n \\ \gamma_n^\dagger \end{pmatrix}. \tag{2.12}
$$

If we calculate the same commutator with the diagonalized Hamiltonian (2.8) using eqs. (2.6) and (2.7), we find

$$
[\Psi_\sigma(\boldsymbol{r}), H] = \sum_{mn}\left[u_{n\sigma}(\boldsymbol{r})\gamma_n + v_{n\sigma}^*(\boldsymbol{r})\gamma_n^\dagger, E_m\gamma_m^\dagger\gamma_m\right] = \sum_n E_n\left(u_{n\sigma}(\boldsymbol{r})\gamma_n - v_{n\sigma}^*(\boldsymbol{r})\gamma_n^\dagger\right), \tag{2.13}
$$

such that we may write

$$
[\Psi(\boldsymbol{r}), H] = \sum_n E_n \begin{pmatrix} u_{n\uparrow}(\boldsymbol{r}) & -v_{n\uparrow}^*(\boldsymbol{r}) \\ u_{n\downarrow}(\boldsymbol{r}) & -v_{n\downarrow}^*(\boldsymbol{r}) \end{pmatrix}\begin{pmatrix} \gamma_n \\ \gamma_n^\dagger \end{pmatrix}. \tag{2.14}
$$

The two expression for $[\Psi(\boldsymbol{r}), H]$ must be equal, for our Bogoliubov transformation to diagonalize H. This restriction determines the wave functions and the energy spectrum of the quasiparticles. The equality is met if we equate coefficients in front of γ_n and $\gamma_n^\dagger$ which gives us the Bogoliubov-de Gennes (BdG) equations.

$$\hat{H}_N(\boldsymbol{r})\begin{pmatrix}u_{n\uparrow}(\boldsymbol{r})\\u_{n\downarrow}(\boldsymbol{r})\end{pmatrix}+\Delta(\boldsymbol{r})\begin{pmatrix}v_{n\downarrow}(\boldsymbol{r})\\-v_{n\uparrow}(\boldsymbol{r})\end{pmatrix}=E_n\begin{pmatrix}u_{n\uparrow}(\boldsymbol{r})\\u_{n\downarrow}(\boldsymbol{r})\end{pmatrix}\tag{2.15a}$$

$$\hat{H}_N(\boldsymbol{r})\begin{pmatrix}v^*_{n\uparrow}(\boldsymbol{r})\\v^*_{n\downarrow}(\boldsymbol{r})\end{pmatrix}+\Delta(\boldsymbol{r})\begin{pmatrix}u^*_{n\downarrow}(\boldsymbol{r})\\-u^*_{n\uparrow}(\boldsymbol{r})\end{pmatrix}=E_n\begin{pmatrix}-v^*_{n\uparrow}(\boldsymbol{r})\\-v^*_{n\downarrow}(\boldsymbol{r})\end{pmatrix}\tag{2.15b}$$

We rewrite (2.15b) in the following way:

$$\begin{aligned}&\sigma_y\hat{H}^*_N(\boldsymbol{r})\sigma_y\sigma_y\begin{pmatrix}v_{n\uparrow}(\boldsymbol{r})\\v_{n\downarrow}(\boldsymbol{r})\end{pmatrix}+\Delta^*(\boldsymbol{r})\sigma_y\begin{pmatrix}u_{n\downarrow}(\boldsymbol{r})\\-u_{n\uparrow}(\boldsymbol{r})\end{pmatrix}=E_n\sigma_y\begin{pmatrix}-v_{n\uparrow}(\boldsymbol{r})\\-v_{n\downarrow}(\boldsymbol{r})\end{pmatrix},\\ \Longrightarrow &-\sigma_y\hat{H}^*_N(\boldsymbol{r})\sigma_y\begin{pmatrix}v_{n\downarrow}(\boldsymbol{r})\\-v_{n\uparrow}(\boldsymbol{r})\end{pmatrix}+\Delta^*(\boldsymbol{r})\begin{pmatrix}u_{n\uparrow}(\boldsymbol{r})\\u_{n\downarrow}(\boldsymbol{r})\end{pmatrix}=E_n\begin{pmatrix}v_{n\downarrow}(\boldsymbol{r})\\-v_{n\uparrow}(\boldsymbol{r})\end{pmatrix}.\end{aligned}\tag{2.16}$$

Using this expression we write the BdG equations as

$$\begin{aligned}\mathcal{H}(\boldsymbol{r})\Phi_n(\boldsymbol{r})&=E_n\Phi_n(\boldsymbol{r}),\\ \mathcal{H}(\boldsymbol{r})&=\begin{pmatrix}\hat{H}_N(\boldsymbol{r})&\Delta(\boldsymbol{r})\\\Delta^*(\boldsymbol{r})&-\sigma_y\hat{H}^*_N(\boldsymbol{r})\sigma_y\end{pmatrix}\end{aligned}\tag{2.17}$$

where $\Phi_n(\boldsymbol{r})=(u_{n\uparrow}(\boldsymbol{r}),u_{n\downarrow}(\boldsymbol{r}),v_{n\downarrow}(\boldsymbol{r}),-v_{n\uparrow}(\boldsymbol{r}))^T$ is a Nambu spinor. Diagonalizing the original Hamiltonian (2.2) has thus been reduced to solving this eigenvalue problem. The eigenvalues E_n are the energies of the quasiparticles while the corresponding eigenvectors are the wave functions.

2.3 Mean field theory and self-consistency

The Hamiltonian given in eq. (2.2) is a mean field approximation of an interacting Hamiltonian H_{int} describing spin independent and local interactions between electrons [5]. This is also the reason why we shouldn't be alarmed by the fact that the particle number is not conserved. In BCS theory, the ground state wave function for the mean field BCS Hamiltonian is, in fact, a superposition of states with different numbers of particles [6].

The characteristic thermal average of mean field theory is hidden away in the pair potential which we state again here:

$$\Delta(\boldsymbol{r})=-\frac{g}{2}\left\langle\Psi_\downarrow(\boldsymbol{r})\Psi_\uparrow(\boldsymbol{r})\right\rangle.\tag{2.18}$$

This is really a self-consistency equation since the expectation value on the RHS depends on $\Delta(\boldsymbol{r})$ itself through the wave functions $u_{n\sigma}(\boldsymbol{r})$ and $v_{n\sigma}(\boldsymbol{r})$ as is evident from our Bogoliubov transformation (2.6) and the BdG equations (2.17).

In BCS theory, superconductivity arises from an interaction between electrons and phonons in the metal [6]. There is an effective attraction between pairs of electrons with time reversal symmetry mediated by phonons leading to the spontaneous formation of Cooper pairs near the Fermi surface. This effective electron-electron interaction is only attractive for electrons with energies within $\hbar\omega_D$ of the Fermi surface and these are the only electrons we should consider since at low temperatures such as the temperatures of ordinary superconducting phases, only the electrons close to the Fermi surface can take part in scattering processes. Here ω_D is the Debye frequency; a characteristic frequency of the phonons. Therefore, the thermal average in eq. (2.18) should only include states with energy less than $\hbar\omega_D$.

We can write eq. (2.18) in terms of $u_{n\sigma}(\boldsymbol{r})$ and $v_{n\sigma}(\boldsymbol{r})$ using our Bogoliubov transformation (2.6) and the mean value rules for the γ-operators (2.9):

$$\begin{aligned}\Delta(\boldsymbol{r}) &= -\frac{g}{2}\sum_{|E_n|,|E_m|\leq\hbar\omega_D}\left\langle\left(u_{n\downarrow}(\boldsymbol{r})\gamma_n + v^*_{n\downarrow}(\boldsymbol{r})\gamma^\dagger_n\right)\left(u_{m\uparrow}(\boldsymbol{r})\gamma_m + v^*_{m\uparrow}(\boldsymbol{r})\gamma^\dagger_m\right)\right\rangle, \\ &= -\frac{g}{2}\sum_{|E_n|\leq\hbar\omega_D} u_{n\downarrow}(\boldsymbol{r})v^*_{n\uparrow}(\boldsymbol{r})\left(1-n_F(E_n)\right) + v^*_{n\downarrow}(\boldsymbol{r})u_{n\uparrow}(\boldsymbol{r})n_F(E_n).\end{aligned} \tag{2.19}$$

For our solution to be self-consistent, the pair potential we use as input to the BdG equations (2.17) should equal the pair potential calculated from the eigenenergies and eigenvectors with eq. (2.19).

2.4 Energy calculation

To uncover whether it's energetically favorable for a system to have a vortex present or not, we compare the total energy of the system in these two cases. The details of the calculation of the total energy are left out, here; what follows is a summary of the important points.[1] The total energy is the expectation value of the physical, interacting Hamiltonian H_{int} mentioned in the beginning of section 2.3 and not the BCS-like Hamiltonian H. We neglected a constant term from the mean field approximation when we wrote the initial Hamiltonian (2.2) which we need to include, i.e. $\langle H_{int}\rangle \simeq \langle H\rangle + E_{MF}$. We also need to

[1] A summary of Hano Sura's note on this topic [7]

keep the constant energy shift E_0 from eq. (2.8) in mind. This means the total energy is given by

$$E_{tot} = \langle H_{int} \rangle = \sum_n E_n \left\langle \gamma_n^\dagger \gamma_n \right\rangle + E_0 + E_{MF} = \sum_n E_n n_F(E_n) + E_0 + E_{MF}, \tag{2.20}$$

$$E_{MF} = \frac{2}{g} \int \mathrm{d}\boldsymbol{r}\, |\Delta(\boldsymbol{r})|^2, \tag{2.21}$$

where, for the parabolic dispersion of the bulk states,

$$E_0 = \frac{1}{2} \sum_{n\sigma} \int \mathrm{d}\boldsymbol{r}\, u_{n\sigma}^*(\boldsymbol{r}) \hat{H}_N(\boldsymbol{r}) u_{n\sigma}(\boldsymbol{r}) + v_{n\sigma}(\boldsymbol{r}) \hat{H}_N(\boldsymbol{r}) v_{n\sigma}^*(\boldsymbol{r}). \tag{2.22}$$

We don't need the total energy of the surface states in this study. These states have a negligible influence on the total energy of the system due to the enormous amount of bulk states in comparison and we treat the bulk and surface states separately in this low energy model. Furthermore, we won't deal with the question of whether vortices may form spontaneously in only the surface layer. The term E_0 stems from the interchange of field operators that don't anti-commute when rewriting the Hamiltonian as

$$H = E_0 + \frac{1}{2} \int \mathrm{d}\boldsymbol{r}\, \Psi^\dagger(\boldsymbol{r}) \mathcal{H}(\boldsymbol{r}) \Psi(\boldsymbol{r}), \tag{2.23}$$

where $\mathcal{H}$ is given in eq. (2.17) and $\Psi(\boldsymbol{r}) = \begin{pmatrix} \Psi_\uparrow(\boldsymbol{r}) & \Psi_\downarrow(\boldsymbol{r}) & \Psi_\downarrow^\dagger(\boldsymbol{r}) & -\Psi_\uparrow^\dagger(\boldsymbol{r}) \end{pmatrix}^T$. We have neglected a boundary term from partial integration and, thus, assumed there to be no current passing through the boundaries of the system. Starting from eq. (2.23), then using the Bogoliubov transformation (2.6), the BdG equations (2.17), and orthonormality relations (A.2), (A.3), it may be shown that H is, in fact, diagonal in the basis of the Bogoliubov quasiparticle operators $\gamma_n^\dagger, \gamma_n$ and equal to the expression in eq. (2.8).

3 Rephrasing the BdG equations

With the theoretical framework in place, we can proceed to solving the BdG equations. The goal of this section is to lay the groundwork for the numerical work by rephrasing the BdG equations. We will separate the angular and radial parts of the wave function and expand the radial part in a basis of eigenfunctions of the kinetic operator. In the main text, we will only consider this derivation in the case of a bulk layer with a magnetic impurity ion. The derivation follows the one given by Jiang et al. [8]. The procedure for the TSS is very similar – details can be found in appendix C.

We control the presence of a vortex in the center of a superconducting layer by the vorticity ν and write $\Delta(\boldsymbol{r}) = |\Delta(\boldsymbol{r})|e^{i\nu\theta}$. For notational simplicity, we write the pairing profile $|\Delta(\boldsymbol{r})| = \Delta(r)$ as a real function which can be both positive and negative. If there is no magnetic flux penetrating the superconductor, $\nu = 0$ and $\Delta(\boldsymbol{r})$ is real. For a single penetrating flux quantum $\Phi_0 = \frac{h}{2e}$ through the vortex core, the pair potential remains single-valued but with a winding phase: $\nu = \pm 1$. The sign of ν depends on the direction of the external magnetic field or the direction of the magnetic moment of the impurity in the case of a quantum anomalous vortex that is spontaneously generated by the magnetic impurity without an external magnetic field [2].

In the gauge in which $\Delta(\boldsymbol{r}) = \Delta(r)e^{i\nu\theta}$, the wave function is single-valued so that $\Phi_n(r, \theta + 2\pi) = \Phi_n(r, \theta)$. We want to work with a real-valued pair potential which is possible if we perform a gauge transformation of the BdG equations (2.17). We use the unitary matrix

$$U = \operatorname{diag}\left(e^{-i\frac{\nu}{2}\theta}, e^{-i\frac{\nu}{2}\theta}, e^{i\frac{\nu}{2}\theta}, e^{i\frac{\nu}{2}\theta}\right) \tag{3.1}$$

to remove the phase of the pair potential. The transformed equations are

$$\begin{gathered}\tilde{\mathcal{H}}(\boldsymbol{r})\Psi_n(\boldsymbol{r}) = E_n\Psi_n(\boldsymbol{r}),\\ \tilde{\mathcal{H}}(\boldsymbol{r}) = U\mathcal{H}(\boldsymbol{r})U^\dagger = \begin{pmatrix} \hat{\tilde{H}}_N(\boldsymbol{r}) & \Delta(r) \\ \Delta(r) & -\sigma_y\hat{\tilde{H}}_N^*(\boldsymbol{r})\sigma_y \end{pmatrix}, \qquad \Psi_n(\boldsymbol{r}) = U\Phi_n(\boldsymbol{r}),\end{gathered} \tag{3.2}$$

where $\hat{\tilde{H}}_N(\boldsymbol{r}) = e^{-i\nu\theta/2}\hat{H}_N(\boldsymbol{r})e^{i\nu\theta/2}$. See appendix B for some details. The transformed wave function satisfies $\Psi_n(r, \theta + 2\pi) = (-1)^\nu\Psi(r, \theta)$. From now on we neglect the vector potential $\boldsymbol{A}$ since we're considering a type-II superconductor in the limit $\lambda \gg \xi$ [8].

3.1 Bulk states

For a bulk layer with a hole-like parabolic band where $\hat{H}_N$ is given by eq. (2.4), we have

$$\tilde{\mathcal{H}}(\boldsymbol{r}) = e^{-i\frac{\nu}{2}\theta\tau_z'}\left[-\tau_z'\left(\frac{p^2}{2m^*} + \varepsilon_f\right) - \lambda_{so}(r)L_z\tau_z'\sigma_z' - m(r)\left(L_z + \frac{\hbar}{2}\sigma_z'\right)\right]e^{i\frac{\nu}{2}\theta\tau_z'} + \Delta(r)\tau_x', \tag{3.3}$$

where we have extended the Pauli matrices to 4×4 matrices indicated by the prime – in particular $\sigma_z' = \begin{pmatrix} \sigma_z & 0 \\ 0 & \sigma_z \end{pmatrix}$ – and defined $\tau_z' = \begin{pmatrix} I & 0 \\ 0 & -I \end{pmatrix}$, $\tau_x' = \begin{pmatrix} 0 & I \\ I & 0 \end{pmatrix}$ as part of a second set of Pauli matrices acting in the particle-hole channel. Here $I = \operatorname{diag}(1, 1)$ is the two-dimensional identity matrix. We used that $-\sigma_y \hat{H}_N^* \sigma_y = -\hat{H}_{kin} - \hat{H}_{soc} + \hat{H}_{ex}$ for the hole-like part to write eq. (3.3) in this way. The sign flips are taken care of by τ_z'.

We note that $\left[e^{-i\nu\theta\tau_z'/2} A e^{i\nu\theta\tau_z'/2}, L_z\right] = e^{-i\nu\theta\tau_z'/2}[A, L_z]e^{i\nu\theta\tau_z'/2}$ for all operators A. Using this, it's straightforward to show that $\left[\tilde{\mathcal{H}}(\boldsymbol{r}), L_z\right] = 0$ since the operators $\tau_x', \tau_z', \sigma_z', p^2$ all commute with L_z. In the real superconductor, however, there would not be continuous rotational symmetry about the z-axis; instead the Hamiltonian should only obey the symmetries of the material. In this low energy continuum model there exist simultaneous eigenstates of $\tilde{\mathcal{H}}$ and L_z such that we may expand our wave function into partial waves for the angular part.

$$\Psi_n(\boldsymbol{r}) = e^{i\mu\theta}\Psi_{n\mu}(r). \tag{3.4}$$

To match the boundary condition $\Psi_n(r, \theta + 2\pi) = (-1)^\nu \Psi(r, \theta)$, we write $\mu = l - \nu/2$ where l is an integer. We solve the BdG equations in a subspace of constant angular momentum such that also the energies are labeled by the 'good' quantum number μ. Inserting this decomposition (3.4) in the BdG equations (3.2) and canceling the phases, we find an equation for the radial part. Note that $p^2 = -\hbar^2\nabla^2 = -\hbar^2(\partial_r^2 + \frac{1}{r}\partial_r + \frac{1}{r^2}\partial_\theta^2)$ and $L_z = -i\hbar\partial_\theta$ in polar coordinates.

$$\begin{split}\Bigg\{\tau_z'\left[\frac{\hbar^2}{2m^* r^2}\left(r^2\partial_r^2 + r\partial_r - \left(\mu + \frac{\nu}{2}\tau_z'\right)^2\right) - \varepsilon_f\right] - \hbar\lambda_{so}(r)\left(\mu + \frac{\nu}{2}\tau_z'\right)\tau_z'\sigma_z' \\ -\hbar m(r)\left[\left(\mu + \frac{\nu}{2}\tau_z'\right) + \frac{\sigma_z'}{2}\right] + \Delta(r)\tau_x'\Bigg\}\Psi_{n\mu}(r) = E_n^\mu \Psi_{n\mu}(r).\end{split} \tag{3.5}$$

We choose to expand $\Psi_{n\mu}(r)$ in a set of orthonormal Bessel functions of the first kind. This is the natural basis to work in since the Bessel functions are eigenfunctions of the ∇^2-operator in polar coordinates.[2] The set of Bessel functions are labeled by l, j and given by

$$\phi_{lj}(r) = \frac{\sqrt{2}}{RJ_{l+1}(\beta_{lj})} J_l\left(\beta_{lj}\frac{r}{R}\right), \tag{3.6}$$

where J_l is the Bessel function of the first kind of order l and β_{lj} is the j'th root of J_l. They form an orthonormal set such that [9]

$$\int_0^R \mathrm{d}r\, r\phi_{li}(r)\phi_{lj}(r) = \delta_{ij}. \tag{3.7}$$

[2]Bessel's equation has the form: $x^2y''(x) + xy'(x) + (x^2 - \nu^2)y(x) = 0$. Compare with eq. (3.5).

To match eq. (3.5), we choose the following expansion:

$$\begin{aligned}\Psi_{n\mu}(r) &= \left[u_{n\mu_1\uparrow}(r), u_{n\mu_1\downarrow}(r), v_{n\mu_{-1}\downarrow}(r), -v_{n\mu_{-1}\uparrow}(r)\right]^T, \\ u_{n\mu_1\sigma}(r) = \sum_{j=1}^{J} u_{n\mu_1 j\sigma}\phi_{\mu_1 j}(r), &\qquad v_{n\mu_{-1}\sigma}(r) = \sum_{j=1}^{J} v_{n\mu_{-1}j\sigma}\phi_{\mu_{-1}j}(r),\end{aligned} \tag{3.8}$$

where $\mu_\tau = \mu + \frac{\nu}{2}\tau$ is an integer. We may expand any reasonable function in the set of Bessel functions since they are the eigenfunctions of a Hermitian operator and thus form a complete set [9]. We are limited computational-wise, however, in that we must choose a finite J when it's time to crunch the numbers. The expansion is chosen such that the Bessel functions are eigenfunctions of the kinetic part and we may use that

$$\begin{aligned}\left(r^2\partial_r^2 + r\partial_r - \left(\mu + \frac{\nu}{2}\tau\right)^2\right)\phi_{\mu_\tau j}(r) &= \frac{\sqrt{2}}{RJ_{\mu_\tau+1}(\beta_{\mu_\tau j})}\left(x^2\partial_x^2 + x\partial_x - \mu_\tau^2\right)J_{\mu_\tau}(x), \\ &= -r^2\left(\frac{\beta_{\mu_\tau j}}{R}\right)^2\phi_{\mu_\tau j}(r),\end{aligned} \tag{3.9}$$

where we changed variables to $x = \beta_{\mu_\tau j}r/R$ and used Bessel's equation (see footnote 2).

Let's introduce a new notation to label the components of the spinor $\Psi_{n\mu}(r)$.

$$\Psi_{n\mu}(r) = \left[\Psi_{n\mu}^{11}(r), \Psi_{n\mu}^{-11}(r), \Psi_{n\mu}^{1-1}(r), \Psi_{n\mu}^{-1-1}(r)\right]^T. \tag{3.10}$$

The components $\Psi_{n\mu}^{\sigma\tau}(r)$ are labeled with $\sigma, \tau = \pm 1$ which have the same values as the entries in the matrices σ_z', τ_z' that match the spinor $\Psi_{n\mu}(r)$. The components are expanded in Bessel functions as given in (3.8).

$$\Psi_{n\mu}^{\sigma\tau}(r) = \sum_{j=1}^{J} f_{n\mu j}^{\sigma\tau}\phi_{\mu_\tau j}(r), \tag{3.11a}$$

$$f_{n\mu j}^{11} = u_{n\mu_1 j\uparrow},\ \ f_{n\mu j}^{-11} = u_{n\mu_1 j\downarrow},\ \ f_{n\mu j}^{1-1} = v_{n\mu_{-1}j\downarrow},\ \ f_{n\mu j}^{-1-1} = -v_{n\mu_{-1}j\uparrow}. \tag{3.11b}$$

Using this notation and eq. (3.9), we write the radial equation (3.5) in the basis of Bessel functions as

$$\begin{aligned}\sum_{j=1}^{J}\left\{-\tau\left[\frac{\hbar^2}{2m^*}\left(\frac{\beta_{\mu_\tau j}}{R}\right)^2 + \varepsilon_f\right] - \hbar\lambda_{so}(r)\mu_\tau\tau\sigma - \hbar m(r)\left(\mu_\tau + \frac{\sigma}{2}\right)\right\} f_{n\mu j}^{\sigma\tau}\phi_{\mu_\tau j}(r) \\ + \sum_{j=1}^{J}\Delta(r) f_{n\mu j}^{\sigma-\tau}\phi_{\mu_{-\tau}j}(r) = \sum_{j=1}^{J} E_n^\mu f_{n\mu j}^{\sigma\tau}\phi_{\mu_\tau j}(r).\end{aligned} \tag{3.12}$$

The top row of the matrix equation (3.5) is equivalent to setting $\sigma = \tau = 1$; second row: $\sigma = -1, \tau = 1$, etc.. Taking the inner product with $\phi_{\mu_\tau i}(r)$ we have

$$\sum_{j=1}^{J} f_{n\mu j}^{\sigma\tau} \int_0^R \mathrm{d}r\, r \left\{ -\tau \left[\frac{\hbar^2}{2m^*} \left(\frac{\beta_{\mu_\tau j}}{R} \right)^2 + \varepsilon_f \right] - \hbar\lambda_{so}(r)\mu_\tau \tau\sigma - \hbar m(r) \left(\mu_\tau + \frac{\sigma}{2} \right) \right\} \phi_{\mu_\tau i}(r) \phi_{\mu_\tau j}(r)$$
$$+ \sum_{j=1}^{J} f_{n\mu j}^{\sigma-\tau} \int_0^R \mathrm{d}r\, r \Delta(r) \phi_{\mu_\tau i}(r) \phi_{\mu_{-\tau} j}(r) = \sum_{j=1}^{J} E_n^\mu f_{n\mu j}^{\sigma\tau} \int_0^R \mathrm{d}r\, r \phi_{\mu_\tau i}(r) \phi_{\mu_\tau j}(r). \quad (3.13)$$

Using the orthonormality relation in eq. (3.7) to simplify the kinetic term and the RHS, we find

$$\sum_{j=1}^{J} \left\{ \left[\tau \left(T_{\mu_\tau}\right)_{ij} - \tau\sigma \left(\Lambda_{\mu_\tau}\right)_{ij} - \left(L_{\mu_\tau}\right)_{ij} - \sigma \left(M_{\mu_\tau}\right)_{ij} \right] f_{n\mu j}^{\sigma\tau} + \left(\Delta_{\mu_\tau, \mu_{-\tau}}\right)_{ij} f_{n\mu j}^{\sigma-\tau} \right\} = E_n^\mu f_{n\mu i}^{\sigma\tau}, \quad (3.14)$$

where the matrix elements are given by

$$(T_\mu)_{ij} = -\left[\frac{\hbar^2}{2m^*} \left(\frac{\beta_{\mu j}}{R} \right)^2 + \varepsilon_f \right] \delta_{ij}, \quad (3.15a)$$

$$[(L_\mu)_{ij}, (M_\mu)_{ij}, (\Lambda_\mu)_{ij}] = \int_0^R \mathrm{d}r\, r \left[\mu\hbar m(r), \frac{1}{2}\hbar m(r), \mu\hbar\lambda_{so}(r) \right] \phi_{\mu i}(r) \phi_{\mu j}(r), \quad (3.15b)$$

$$\left(\Delta_{\mu,\mu'}\right)_{ij} = \int_0^R \mathrm{d}r\, r \Delta(r) \phi_{\mu i}(r) \phi_{\mu' j}(r). \quad (3.15c)$$

We write eq. (3.14) as a $4J \times 4J$ eigenvalue problem for each angular momentum value.

$$\begin{pmatrix} (T-L-M-\Lambda)_{\mu_1} & 0 & \Delta_{\mu_1 \mu_{-1}} & 0 \\ 0 & (T-L+M+\Lambda)_{\mu_1} & 0 & \Delta_{\mu_1 \mu_{-1}} \\ \Delta_{\mu_1 \mu_{-1}}^T & 0 & -(T+L+M-\Lambda)_{\mu_{-1}} & 0 \\ 0 & \Delta_{\mu_1 \mu_{-1}}^T & 0 & -(T+L-M+\Lambda)_{\mu_{-1}} \end{pmatrix} \Psi_{n\mu} = E_n^\mu \Psi_{n\mu}, \quad (3.16)$$

where $\Psi_{n\mu} = [u_{1\uparrow}, ..., u_{J\uparrow}, u_{1\downarrow}, ..., u_{J\downarrow}, v_{1\downarrow}, ..., v_{J\downarrow}, ..., -v_{1\uparrow}, ..., -v_{J\uparrow}]^T$ with suppressed indices n, μ_τ.

Solving the BdG equations to find the energy spectrum of the Bogoliubov quasiparticles and the corresponding wave functions boils down to solving eq. (3.16) or eq. (C.15) for a bulk layer with a magnetic impurity or a TSS in the vicinity of such an impurity. This amounts to determining the eigenvalues and eigenvectors of the matrix on the LHS of these equations. For the bulk layer, the pair potential needs to be self-consistent (cf. section 2.3). This is not the case for the TSS where superconductivity is proximity-induced by the bulk material.

4 Anomalous vortices and zero-energy bound states

Now that we have rephrased the BdG equations, we move on to the numerical solution of these. The process will be similar to the one outlined in the QAV-paper. We choose the same material parameters as they use to model Fe(Te,Se) superconductors. The electronic dispersion is described by a hole-like parabolic band around the Γ-point with effective mass $m^* \simeq 4.08 m_e$ and Fermi energy $\varepsilon_f \simeq -4.52\,\mathrm{meV}$ for the bulk states (m_e is the electron mass). The bulk value of the superconducting gap far from impurities and vortices is $\Delta = 1.5\,\mathrm{meV}$. We choose $g = 69\,\mathrm{meV}$ and $\hbar\omega_D = 4.7\,\mathrm{meV}$ to match this value.[3] For the TSS, we use the parameters $\hbar v_D = 0.216\,\mathrm{eV{\cdot}\AA}$ and $\varepsilon'_f = 4.5\,\mathrm{meV}$. All equations and parameters are written in dimensionless form by introducing an energy scale of 10 meV and the corresponding length scale l_0 defined by $\frac{\hbar^2}{2m^* l_0^2} = 10\,\mathrm{meV} \implies l_0 = 0.966\,\mathrm{nm}$. Energies and lengths will be expressed in these units unless otherwise stated. The radius of superconducting disc needs to be significantly larger than the coherence length ξ and range of all impurity effects. The BCS coherence length [2] $\xi_{BCS} = \frac{\hbar v_F}{\pi\Delta} \simeq 2.76\,\mathrm{nm} = 2.86 l_0$ gives us an estimate of the true coherence length of the material. We choose $R = 250$ for the disc radius.

The wave functions are normalized such that the orthonormality relations in eqs. (A.2), (A.3) are satisfied. Actually, (A.3) will always be satisfied due to the integral over the angular part $e^{2i\mu\theta}$. Using the expansion (3.11a) for the bulk states or (C.8b) for the surface states and the orthonormality of the Bessel functions (3.7), we write (A.2) as

$$\int \mathrm{d}\boldsymbol{r} \sum_{\sigma} u_{n\sigma}(\boldsymbol{r}) u^*_{m\sigma}(\boldsymbol{r}) + v_{n\sigma}(\boldsymbol{r}) v^*_{m\sigma}(\boldsymbol{r}) = 2\pi \sum_{\sigma\tau j} f^{\sigma\tau}_{n\mu j} f^{\sigma\tau}_{m\mu j} = \delta_{nm}, \tag{4.1}$$

which we explicitly check numerically.

As previously mentioned, we use a finite number J of functions in the basis of Bessel functions. It is often enough to set $J = 100$ to find self-consistent solutions but all the results given here are generated with $J = 200$. This cutoff determines the spatial resolution of the wave functions and thereby the pair potential. We also use a cutoff in the number of angular momenta channels such that only channels with $|\mu| < L_C$ are considered. Note that the normalized Bessel functions are symmetric under inversion of angular momentum, i.e. $\phi_{lj}(r) = \phi_{-lj}(r)$. This limits numerical calculations to only non-negative values of angular momentum. See appendix D for details.

[3] This value of g is 2π times greater than the attraction strength used in the QAV-paper. It might be due to a different wave function normalization.

A self-consistent solution is ensured by an iterative process. Initially, a guess of the pair potential is used to calculate the matrix from the BdG equations (3.16) or (C.15). Then, the matrix is diagonalized and the eigenvalues and eigenvectors are used to update the pairing profile using eq. (2.19) ($\Delta_{old}(r) \to \Delta_{new}(r)$). The new pairing profile is used to update the matrix before it's diagonalized again, and so on. The self-consistency process continues until the pairing profile has converged. The convergence criteria is met when

$$\int_0^R \mathrm{d}r \, |\Delta_{new}(r) - \Delta_{old}(r)| < \alpha. \tag{4.2}$$

We choose $\alpha = 0.001$ as the convergence measure. The results seem to be insensitive to the initial guess but a better guess needs fewer iterations before convergence is reached.

In experiments with scanning tunneling microscopy (STM), it's possible to measure the tunneling conductance between the tip of the STM apparatus and the material in question. This quantity is proportional to the local density of states (LDOS) which we calculate as [8]

$$\frac{\mathrm{d}I}{\mathrm{d}V}(r, V) \propto \sum_{n\mu\sigma} u^2_{n\mu\sigma}(r) n'_F(E^\mu_n - eV) + v^2_{n\mu\sigma}(r) n'_F(E^\mu_n + eV), \tag{4.3}$$

where eV is the bias energy and $n'_F(E)$ is the derivative of the Fermi-Dirac distribution.

4.1 Normal vortex in a bulk layer

In the simplest case of no magnetic impurity in a bulk layer with no vortex present, we find a homogeneous self-consistent pair potential and a gap of 2Δ in the energy spectrum and LDOS around the Fermi surface, as we would expect. This is shown in fig. 4.1(a-c). $\Delta(r)$ drops off around $r = 150$ owing to the angular momentum cutoff $L_C = 150$. This is purely a numerical problem along with the strong oscillations at the boundary; they have no physical justifications. As shown with the dashed line, we use an average bulk value to extrapolate and fix $\Delta(r > 50) = \Delta_{bulk} = 1.49$ meV in all other calculations.

Adding a vortex to the system as shown in fig. 4.1(d-f), the pairing profile is zero in the core and increases linearly, initially, before oscillating and reaching the bulk value for $r > 20$. The energy spectrum shows in-gap Caroli-de Gennes-Matricon (CdGM) bound states whose energies $E^\mu = \pm 0.36, \pm 0.66, \pm 0.84, \ldots$ meV are fairly close to the approximate energies $\mu \frac{\Delta^2_{bulk}}{\varepsilon_f} = \pm 0.25, \pm 0.74, \pm 1.23, \ldots$ meV of CdGM states [10]. The expression is given in the limit $E^\mu \ll \Delta_{bulk}$, however, which is only valid for the first energy levels.

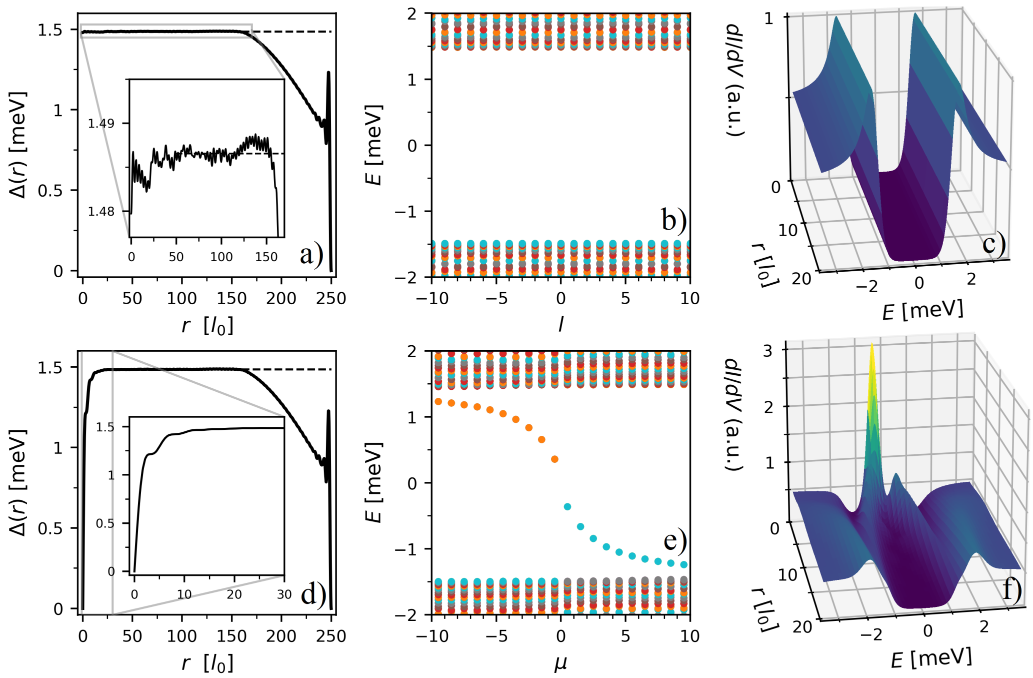

Figure 4.1: Bulk layer with no magnetic impurity ($J = 200$, $L_C = 150$). Top row: no vortex ($\nu = 0$), bottom row: vortex present at $r = 0$ ($\nu = -1$). (a,d) Self-consistent pairing profile $\Delta(r)$; dashed line shows the extrapolated cutoff value. Insets in (a,d) show zoomed in views in the same units as (a,d) themselves. (b,e) Energy level spectrum showing spin-degenerate states. (c,f) 3-D plot of the LDOS as a function of bias energy along a line through the center of the disc calculated at $T = 1.5$ K. Note that the energy spectra and LDOS are calculated with the pairing profile cutoff.

Wave functions for some of the vortex core bound states are found in fig. E.1. All states in the energy spectra are doubly degenerate since, at this point, we have not included spin-dependent effects. The LDOS is strongly peaked in the vortex core at $E = -0.36$ meV before two symmetrically spaced ridges emerge when moving away from the core.[4] The core peak can almost be entirely attributed to the four bound states at $\mu = \pm\frac{1}{2}$. The asymmetry at $r = 0$ stems from the fact that for $\mu = -\frac{1}{2}$, only $v_{n\mu\sigma}(r = 0)$ is nonzero, while for $\mu = +\frac{1}{2}$, only $u_{n\mu\sigma}(r = 0)$ is nonzero and the Fermi terms on u, v in eq. (4.3) come with opposite signs in the bias energy.

We noticed that L_C should be picked with some caution due to boundary effects. The bound states with very high angular momentum live close to the edge of the disc. Their wave functions should extend beyond the edge but we are effectively cutting them off and forcing them to vanish at the edge (see the right column of fig. E.1) due to the way the Bessel functions are normalized ($\phi_{lj}(r = R) = 0$). We treat all states as if they lie within the edge of the disc and this large alteration of wave functions leads to undesirable boundary effects. We want to include as many CdGM bound states as possible for energy comparisons but also keep the extent of boundary effects to a minimum. With this in mind, we choose $L_C = 100$ as the angular momentum cutoff going forward (see also fig. E.2). This cutoff does not affect the pair potential below its cutoff point $r = 50$.

4.2 Quantum anomalous vortex in a bulk layer

Now that we have discussed the normal case, we add the magnetic impurity ion to the system. In the QAV-paper they find that above a critical exchange interaction strength $\hbar m_0^c \simeq 6.1$ meV and with strong SOC, a quantum anomalous vortex may spontaneously nucleate around the impurity. They use parameters $\hbar\lambda_0 = 6.6$ meV and $r_0 = 2$ to model the interaction with the impurity (see eq. (2.4)). We will reproduce the calculation here and compare results.

The vortex may be generated spontaneously, meaning without an external magnetic field, if the total energy of the system in the vortex phase E_{vortex} is lower than in the normal phase $E_{vortex-free}$. We define the vortex binding energy as

$$E_{vb} = E_{vortex} - E_{vortex-free}. \tag{4.4}$$

[4] The symmetrically spaced ridges were found in experiments by Hess et al. [11] in 1990 and calculated numerically by Gygi and Schlüter [12] a short time thereafter.

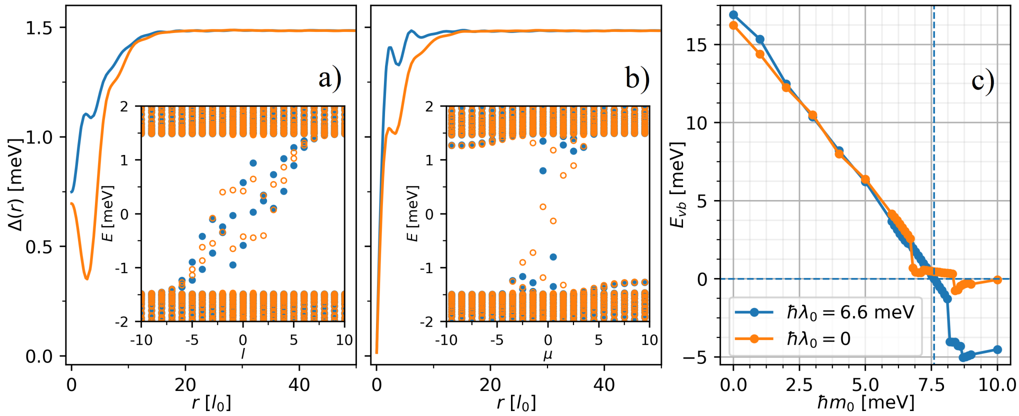

Figure 4.2: Bulk layer with magnetic impurity ($J = 200$, $L_C = 100$). Blue lines/dots: with SOC ($\hbar\lambda_0 = 6.6$ meV); orange lines/dots: without SOC ($\hbar\lambda_0 = 0$). (a,b) Self-consistent pairing profile with $\hbar m_0 = 8.0$ meV (Inset: corresponding energy level spectrum). Vortex present in (b) ($\nu = -1$), not in (a) ($\nu = 0$). (c) Vortex binding energy as a function of the exchange interaction strength m_0 showing a critical value $\hbar m_0^c \simeq 7.6$ meV for the case with strong SOC.

The process is spontaneous if $E_{vb} < 0$. We calculate the total energy of the system using eq. (2.20). For the normal situation considered in section 4.1 without a magnetic impurity, $E_{vb} = +16$ meV and an external magnetic field is required to generate the vortex. The pair potential vanishes in the vortex core, reducing the mean field correction term E_{MF} compared to the vortex-free phase. This, however, is not enough for $E_{vb} < 0$ since all states below the Fermi level are occupied and the CdGM states are raised in energy compared to the scattering states in the vortex-free phase that would otherwise be filled. E_0 is the same for both phases in this case and negligible in almost all other cases, too.

We find the same qualitative results as in the QAV-paper when we add the magnetic impurity which we will compare to the system without one (fig. 4.1). In the vortex-free state shown in fig. 4.2(a), we see that the pair potential has been heavily suppressed near the ion – more so for the case without SOC that displays a large dip. We find so-called Yu-Shiba-Rusinov (YSR) in-gap bound states which are well-known defect excitations in superconductors with magnetic impurities [13–15]. This raises the energy of the vortex-free state compared to without the impurity even though the mean field term E_{MF} is smaller since the pair potential is suppressed.

In the vortex state (fig. 4.2(b)), the pairing profile with SOC shows enhanced oscillations compared to the case without the impurity; the pairing profile without SOC is more suppressed as in the vortex-free case. We see some YSR in-gap bound states just inside the superconducting gap besides the CdGM states which have been pushed away from the Fermi level. The exchange interaction $\hat{H}_{ex} = -m_0 e^{-r/r_0} J_z$ lowers (raises) the energy of the states with $j_z > 0$ ($j_z < 0$) for $m_0 > 0$. The effect is largest for the states with small angular momentum due to the exponential decay. The vorticity $\nu = -1$ is such that the CdGM states have the right 'chirality' $\mathrm{sgn}(\varepsilon_f)\nu > 0$ [2] and the exchange interaction lowers the energy of the occupied states. Without SOC, the two CdGM states with $j_z = 0$ are only affected through the changed pair potential. From fig. F.1 showing the individual energies of the two different states, we note that the decrease in binding energy is mainly due to a decrease in the energy of the vortex state.

As shown in fig. 4.2(c), there exists a range of exchange interaction strengths, starting from the critical value $\hbar m_0^c \simeq 7.6$ meV – not far from the value reported in the QAV-paper – where quantum anomalous vortices may form in the bulk material with strong SOC. Comparing the results with and without SOC, the stability of the vortex phase is clearly helped by strong SOC – without SOC, E_{vb} just barely becomes negative. The existence of a critical value m_0^c depends on both the strength of the SOC and the interaction range r_0. The binding energy for other parameter choices is shown in fig. F.2. We find that SOC is not needed if the decay length is longer ($r_0 = 4$ was tested) but the vortex state is not favored if the decay length is shorter ($r_0 = 1$ was tested).

There seems to be an almost linear relation between E_{vb} and m_0 until some other critical interaction strength $m_0^{c\prime}$ when the first YSR state of the vortex-free phase crosses the Fermi level which is correlated with a phase transition-like change of the pair potential that makes E_{vb} jump discontinuously. For $m_0 > m_0^{c\prime}$, the energy of the vortex-free state doesn't change in a simple increasing manner as seen in fig. F.1 and the binding energy depends in a complicated fashion on m_0. To fully understand the non-linear regime $m_0 > m_0^{c\prime}$, we would need to study both the energy spectrum of the YSR states and the correlation between Fermi level crossings of bound states and discontinuous changes in the pair potential in much greater detail which is beyond the scope of this thesis (see appendix G for preliminary notes on the second topic). We note, however, that SOC pushes the low angular momentum YSR states away from the Fermi level, leading to a larger $m_0^{c\prime}$ for the system with SOC and, eventually, to a more favorable vortex state.

4.3 Anomalous vortices in superconductors with (anti-)ferromagnetic exchange interactions

Now that we have seen that a vortex may nucleate spontaneously in the bulk layers around a magnetic impurity with simple exponential decay as the FM exchange interaction, we investigate whether other types of exchange interaction may produce anomalous vortices as well. We omit SOC for simplicity. It was found with neutron scattering experiments by Thampy et al. [16] that an interstitial Fe impurity in Fe(Te,Se) induces Friedel-like oscillations in the magnetic alignment of more than 50 neighboring Fe sites, motivating us to try an AFM exchange interaction of the form $m(r) = m_0 \cos(kr) e^{-r/r_0}$. We keep the range at $r_0 = 2$ and extract the wave number $k = 8\ \mathrm{nm}^{-1}$ from the experiment.

Our results are gathered in fig. H.1 for these and other parameters. We find that it does not give rise to anomalous vortices in the hole-like parabolic band – even for wavelengths 8 times longer, making it more similar to the previous case with $m(r) = m_0 e^{-r/r_0}$. The vortex binding energy does decrease as m_0 is increased but not in a simple linear form and not enough for the vortex state to be favorable for the parameters considered here. We have seen that a crucial element to generating anomalous vortices is pushing the CdGM states away from the Fermi level. With the AFM exchange coupling considered here, this is done inefficiently since $\hat{H}_{ex} = -m(r) J_z$ only lowers the energy of some occupied CdGM states while raising the energy of others due to oscillatory coupling.

Instead, we turn our attention to the investigation of whether a different shape of the exchange coupling also makes the vortex state favorable for FM exchange interactions. We try a circular FM island/puddle of aligned magnetic moments of radius r', modeled by a Fermi function with smooth decay at the edge of the island: $m(r) = m_0 \frac{1}{2}\left(1 - \tanh\left(\frac{r-r'}{0.4 l_0}\right)\right)$. Three different radii $r' = 2, 5, 10$ have been tested and the results are shown in fig. H.2. We find that a radius of $r' = 10$ gives rise to spontaneous vortex formation for a range of exchange interaction strengths $0.5\ \mathrm{meV} \lesssim \hbar m_0 \lesssim 0.7\ \mathrm{meV}$.

Studying the energy spectra for the vortex and vortex-free states in the bulk layer in fig. H.4 and H.3, respectively, we can explain the initial decrease in binding energy seen in fig. H.2(c-d) with similar arguments as in section 4.2. YSR-like bound states in band-like structures raise the energy of the vortex-free state compared to zero exchange field. Meanwhile, the CdGM states are pushed away from the Fermi level, lowering the energy of the vortex state. The $j_z = 0$ CdGM states are only affected through the changing pair potential. The YSR-like states play a significantly larger role in the vortex state than what

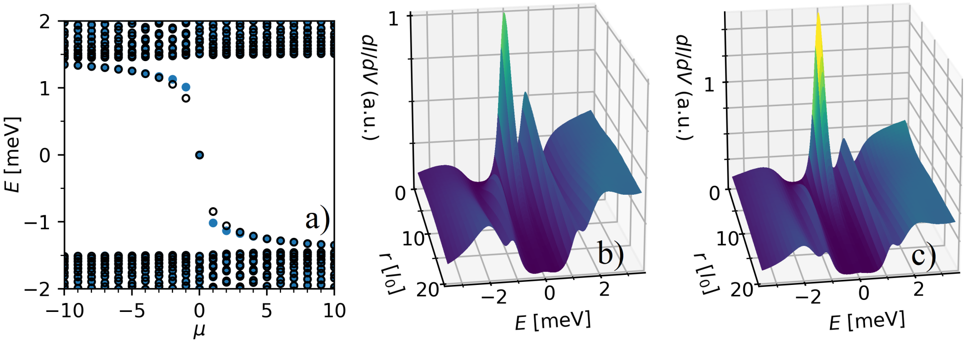

Figure 4.3: Surface layer in the vortex state. (a) Energy level spectrum – open, black circles: without magnetic impurity; filled blue circles: $\hbar m_0 = 8.0$ meV, $\hbar\lambda_0 = 6.6$ meV, $r_0 = 2$. (b,c) LDOS along a line through the center of the disc calculated at $T = 1.5$ K. Magnetic impurity present in (c); no impurity in (b).

is seen in fig. 4.2(b) with the exponentially decaying exchange coupling, however. This could account for the less steep energy decrease of the vortex state. As is evident from fig. H.2(d), the initial decrease in binding energy seen in fig. H.2(c) is, to a larger degree, a joint effort between the vortex and vortex-free states. At the minimum of E_{vb}, the energy of the vortex state is lowered by about the same amount as the vortex-free state increases in energy. The mean field term does not change the binding energy significantly but does lower the total energy of both states due to the suppression of the pair potential.

The energy spectra of the TSS do also contain some in-gap bound states introduced by the exchange interaction but the surface states are affected to a smaller degree by the impurity. In-gap states are most noticeable in the vortex-free state similar to the parabolic band. The CdGM states in the vortex state are only affected very slightly.

4.4 Majorana zero-energy bound state in TSS

We consider now a surface layer – in the vicinity of a magnetic impurity – coupled to the quantum anomalous vortex in the bulk layer due to proximity-induced superconductivity. Therefore, we take the pair potential $\Delta'(\boldsymbol{r})$ to be the self-consistent bulk layer pair potential whose pairing profile $\Delta_{QAV}(r)$ is shown in fig. 4.2(b) (blue curve), i.e. $\Delta'(\boldsymbol{r}) = \Delta_{QAV}(r)e^{i\theta}$.[5] We find a zero-energy bound state (ZBS) among the CdGM states since μ now takes integer values in the vortex state due to the extra Berry phase from the

[5]The vorticity $\nu' = 1$ has opposite sign from the bulk layer case in section 4.2 to preserve the chiralilty of the CdGM states. [2]

changed kinetic part of the Hamiltonian (see appendix C). The energy level spectrum given in fig. 4.3(a) compares it to the case without the magnetic impurity. The impurity has a similar effect of pushing CdGM states away from the Fermi level. Compared to the bulk layer, however, the effect is not as strong in the surface layer. Note also that only the bound states with nonzero angular momentum are affected; the ZBS stays put. This isolates the ZBS from the other bound states which is also evident from the LDOS (fig. 4.3(b-c)).

Numerically, there are actually two degenerate ZBSs (in both the case with and without the impurity) with energies $E^{\pm} = \pm 10^{-4}$ meV with which we form the linear combinations $\Psi^{+}(\boldsymbol{r}) = \frac{1}{\sqrt{2}}\left(\Psi_{E^+}(\boldsymbol{r}) + \Psi_{E^-}(\boldsymbol{r})\right)$ and $\Psi^{-}(\boldsymbol{r}) = \frac{1}{\sqrt{2}}\left(\Psi_{E^+}(\boldsymbol{r}) - \Psi_{E^-}(\boldsymbol{r})\right)$. From the wave functions depicted in fig. I.1, we see that $\Psi^{+}(\boldsymbol{r})$ is an edge state while $\Psi^{-}(\boldsymbol{r})$ is a localized charge neutral Majorana zero-mode since it satisfies $\gamma^{\dagger} = \gamma$ [8].[6] The vortex core bound states of the helical Dirac fermion TSS have previously been studied analytically without the magnetic impurity by Deng et al. [3] where they found the Majorana mode, we also see here, numerically. They also give an approximate expression for the bound state energies identical to the CdGM result for the parabolic band: $E^{\mu} \simeq \mu \frac{\Delta_{bulk}^2}{\varepsilon_f} = 0, \pm 0.49, \pm 0.99, ...$ meV which is not quite as close to the numerical result $E^{\mu} = 0, \pm 0.81, \pm 1.0, ...$ meV as the CdGM states in section 4.1. The energies of the bound states with non-zero angular momentum are, however, closer to $\Delta_{bulk} = 1.5$ meV which could account for the larger difference.

4.5 Zeeman splitting of Majorana mode and tuned YSR states

A vortex in the TSS is not the only way to produce a ZBS. By tuning the strength of the exchange interaction, it's possible to find YSR bound states with zero energy in a vortex-free state. This is true for both the parabolic bulk band and helical Dirac fermion TSS. The tuned YSR states do not share the robustness of the protected Majorana mode, though, due to the finicky nature of the tuning. The energy of the Majorana mode is not affected by the presence of an impurity as we saw in section 4.4. We turn off the SOC and choose a smaller exchange interaction range $r_0 = 0.5$ to isolate the ZBS. For the bulk band, the tuned interaction strength is $m_0 = m_0^{c\prime\prime} = 61.7$ meV and $m_0 = 229$ meV for the TSS. For these values, the two $l = 0$ YSR states are calculated to have zero energy.

We calculate the Zeeman splitting by an external magnetic field $\boldsymbol{B} = B_z\hat{\boldsymbol{z}}$ parallel to the impurity moment by adding the term $\hat{H}_Z = -\boldsymbol{\mu} \cdot \boldsymbol{B} \simeq -\mu_B \sigma_z B_z$ to the normal part of

[6] Expressions for the quasiparticle operators are given in eq. (A.1). The condition $\gamma^{\dagger} = \gamma$ is satisfied if $u_{\uparrow}(r) = v_{\uparrow}(r)$ and $u_{\downarrow}(r) = v_{\downarrow}(r)$ which is the case for $\Psi^{-}(\boldsymbol{r})$ (see fig. I.1).

the Hamiltonian $\hat{H}_N$, assuming a g-factor of $g \simeq 2$. We treat this as a perturbation to the zero-field Hamiltonian meaning that the pair potential is not self-consistent when $B_z \neq 0$. We find that the zero-bias peak generated by the tuned YSR states in a LDOS measurement of both bulk and surface layers shifts when an external magnetic field is applied to the tuned YSR ZBS in contrast to the Majorana mode which stays pinned at zero bias (see figs. J.1 and J.2). Thus, these two different ZBSs should be easily discerned in experiments. The Zeeman splitting in the TSS is smaller than bulk layers since the tuning value is greater and thus a magnetic field of the same strength will have a smaller effect.

This perturbative approach does, however, cause some concern for the bulk YSR states, specifically, since the system is tuned to a 'phase transition' ($m_0 = m_0^{c\prime\prime}$) where the pair potential changes discontinuously for stronger exchange interactions (see appendix G and figs. G.1 and G.3 in particular). The added magnetic field has a similar effect since we're effectively transforming the matrix element $(M_\mu)_{ij} \to (M_\mu)_{ij} + \mu_B B_z \delta_{ij}$. A self-consistent solution does, nevertheless, lead to the same conclusion; that the bulk YSR ZBSs split in an external magnetic field, but they do so discontinuously if the field is parallel with $\boldsymbol{I}_{imp}$, forcing the transition, and continuously if the field is anti-parallel (see fig. J.3).

5 Conclusion

We have used the Bogoliubov-de Gennes (BdG) formalism and the theoretical model by Jiang et al. [2] (QAV-paper) to numerically study s-wave superconductors with a hole-like parabolic band for bulk states and helical Dirac fermion topological surface states in which superconductivity is induced via a proximity effect, modeling iron-based Fe(Te,Se) superconductors around the Γ-point. We have reproduced and studied some of the results by Jiang et al. and found qualitative agreement with these. We find that the exchange interaction from a single magnetic impurity $\hat{H}_{ex} = -m_0 e^{-r/r_0} J_z$ such as an interstitial Fe atom gives rise to a spontaneous vortex generation at the site of the impurity if the interaction strength m_0 is in a certain critical range and the superconductor has strong SOC or long-ranged exchange coupling. The effect of the exchange interaction is two-fold: i) it pushes CdGM vortex core bound states away from the Fermi level, lowering the energy of the vortex state and ii) introduces in-gap YSR bound states to the vortex-free state, raising the energy of that state. The combined effect is a decreased vortex binding energy.

Additionally, we have studied other exchange interactions: antiferromagnetic $\hat{H}_{ex} = -m_0 \cos(kr) e^{-r/r_0} J_z$ which did not lead to anomalous vortices and extended ferromagnetic islands $\hat{H}_{ex} = -m_0 \frac{1}{2}\left(1 - \tanh\left(\frac{r-r'}{0.4l_0}\right)\right) J_z$ for which there exists a range of interaction strengths m_0 where spontaneous vortex formation occurs given a large enough radius $r' = 10$.

We have also studied different zero energy bound states. Coupling the quantum anomalous vortex of the bulk states to the TSS we find a Majorana zero mode among the CdGM bound states. We find this bound state to be more isolated in the presence of a magnetic impurity ion in agreement with the QAV-paper. By tuning the exchange interaction strength its possible to find YSR ZBSs in the vortex-free state in both the parabolic band and the TSS. We find that the tuned YSR ZBSs split in a external magnetic field due to the Zeeman effect but the Majorana zero mode does not. The YSR ZBSs in the TSS show a smaller splitting with the same magnetic field strength than in the parabolic band due to a much higher exchange interaction tuning value.

Further research into this topic could involve looking into other shapes for the exchange coupling or a detailed analysis of the correlation between Fermi level crossings of bound states and discontinuous changes in the pair potential which we have observed. This would perhaps lead to a deeper understanding of how the the total energy of the vortex-free state dependends on the exchange interaction strength.

Appendices

A Bogoliubov quasiparticle operators

In this section we will prove that the inverted expressions for the Bogoliubov quasiparticle operators $\gamma_n^\dagger, \gamma_n$ are given by [8]

$$\gamma_n^\dagger = \int \mathrm{d}\boldsymbol{r} \sum_\sigma u_{n\sigma}(\boldsymbol{r})\Psi_\sigma^\dagger(\boldsymbol{r}) + v_{n\sigma}(\boldsymbol{r})\Psi_\sigma(\boldsymbol{r}), \tag{A.1a}$$

$$\gamma_n = \int \mathrm{d}\boldsymbol{r} \sum_\sigma u_{n\sigma}^*(\boldsymbol{r})\Psi_\sigma(\boldsymbol{r}) + v_{n\sigma}^*(\boldsymbol{r})\Psi_\sigma^\dagger(\boldsymbol{r}), \tag{A.1b}$$

when we use the Bogoliubov transformation of eq. (2.6). We will prove this by ensuring that the left and right hand sides of eq. (A.1) are equal when the original Bogoliubov transformation (2.6) for $\Psi_\sigma, \Psi_\sigma^\dagger$ is used. To this end, we need two other results. Previously, we asserted that the Bogoliubov quasiparticles are fermions and, therefore, that $\gamma_n^\dagger, \gamma_n$ should obey the anti-commutation relations in eq. (2.7).

Suppose that eqs. (A.1) are true statements; that $\gamma_n^\dagger, \gamma_n$ really can be expressed in that way. Then

$$\begin{aligned}
\left\{\gamma_n^\dagger, \gamma_m\right\} &= \int \mathrm{d}\boldsymbol{r} \int \mathrm{d}\boldsymbol{r}' \sum_{\sigma\sigma'} \left\{u_{n\sigma}(\boldsymbol{r})\Psi_\sigma^\dagger(\boldsymbol{r}) + v_{n\sigma}(\boldsymbol{r})\Psi_\sigma(\boldsymbol{r}), u_{m\sigma'}^*(\boldsymbol{r}')\Psi_{\sigma'}(\boldsymbol{r}') + v_{m\sigma'}^*(\boldsymbol{r}')\Psi_{\sigma'}^\dagger(\boldsymbol{r}')\right\} \\
&= \int \mathrm{d}\boldsymbol{r} \int \mathrm{d}\boldsymbol{r}' \sum_{\sigma\sigma'} u_{n\sigma}(\boldsymbol{r})u_{m\sigma'}^*(\boldsymbol{r}')\left\{\Psi_\sigma^\dagger(\boldsymbol{r}), \Psi_{\sigma'}(\boldsymbol{r}')\right\} + v_{n\sigma}(\boldsymbol{r})v_{m\sigma'}^*(\boldsymbol{r}')\left\{\Psi_\sigma(\boldsymbol{r}), \Psi_{\sigma'}^\dagger(\boldsymbol{r}')\right\}, \\
&= \int \mathrm{d}\boldsymbol{r} \sum_\sigma u_{n\sigma}(\boldsymbol{r})u_{m\sigma}^*(\boldsymbol{r}) + v_{n\sigma}(\boldsymbol{r})v_{m\sigma}^*(\boldsymbol{r}) \stackrel{!}{=} \delta_{nm},
\end{aligned} \tag{A.2}$$

and

$$\begin{aligned}
\left\{\gamma_n^\dagger, \gamma_m^\dagger\right\} &= \int \mathrm{d}\boldsymbol{r} \int \mathrm{d}\boldsymbol{r}' \sum_{\sigma\sigma'} \left\{u_{n\sigma}(\boldsymbol{r})\Psi_\sigma^\dagger(\boldsymbol{r}) + v_{n\sigma}(\boldsymbol{r})\Psi_\sigma(\boldsymbol{r}), u_{m\sigma'}(\boldsymbol{r}')\Psi_{\sigma'}^\dagger(\boldsymbol{r}') + v_{m\sigma'}(\boldsymbol{r}')\Psi_\sigma(\boldsymbol{r}'))\right\} \\
&= \int \mathrm{d}\boldsymbol{r} \sum_\sigma u_{n\sigma}(\boldsymbol{r})v_{m\sigma}(\boldsymbol{r}) + v_{n\sigma}(\boldsymbol{r})u_{m\sigma}(\boldsymbol{r}) \stackrel{!}{=} 0,
\end{aligned} \tag{A.3}$$

must also be satisfied; otherwise $\gamma_n^\dagger, \gamma_n$ as given in eq. (A.1) wouldn't represent fermionic particles.

Inserting eq. (2.6) in the RHS of eq. (A.1a) and using eqs. (A.2) and (A.3), we have

$$\begin{aligned}
&\int \mathrm{d}\boldsymbol{r} \sum_{\sigma} u_{n\sigma}(\boldsymbol{r})\Psi_{\sigma}^{\dagger}(\boldsymbol{r}) + v_{n\sigma}(\boldsymbol{r})\Psi_{\sigma}(\boldsymbol{r}) \\
&= \int \mathrm{d}\boldsymbol{r} \sum_{m\sigma} \left[u_{n\sigma}(\boldsymbol{r})u_{m\sigma}^{*}(\boldsymbol{r}) + v_{n\sigma}(\boldsymbol{r})v_{m\sigma}^{*}(\boldsymbol{r})\right]\gamma_m^{\dagger} + \left[u_{n\sigma}(\boldsymbol{r})v_{m\sigma}(\boldsymbol{r}) + v_{n\sigma}(\boldsymbol{r})u_{m\sigma}(\boldsymbol{r})\right]\gamma_m, \\
&= \gamma_n^{\dagger}.
\end{aligned} \tag{A.4}$$

Similarly for the RHS of eq. (A.1b), we have

$$\begin{aligned}
&\int \mathrm{d}\boldsymbol{r} \sum_{\sigma} u_{n\sigma}^{*}(\boldsymbol{r})\Psi_{\sigma}(\boldsymbol{r}) + v_{n\sigma}^{*}(\boldsymbol{r})\Psi_{\sigma}^{\dagger}(\boldsymbol{r}) \\
&= \int \mathrm{d}\boldsymbol{r} \sum_{m\sigma} \left[u_{n\sigma}^{*}(\boldsymbol{r})u_{m\sigma}(\boldsymbol{r}) + v_{n\sigma}^{*}(\boldsymbol{r})v_{m\sigma}(\boldsymbol{r})\right]\gamma_m + \left[u_{n\sigma}^{*}(\boldsymbol{r})v_{m\sigma}^{*}(\boldsymbol{r}) + v_{n\sigma}^{*}(\boldsymbol{r})u_{m\sigma}^{*}(\boldsymbol{r})\right]\gamma_m^{\dagger}, \\
&= \gamma_n.
\end{aligned} \tag{A.5}$$

Here we have used the results from Hermitian conjugating eqs. (A.2) and (A.3). Thus, we reach the conclusion that the inverted expressions for $\gamma_n^{\dagger}, \gamma_n$ given in eq. (A.1) are, in fact, consistent with the Bogoliubov transformation defined in eq. (2.6).

B Gauge transforming the BdG equations

In this section we want to prove that the wave function $\Phi_n(\boldsymbol{r})$ and the gap pair potential $\Delta(\boldsymbol{r})$ transform as

$$\Phi_n(\boldsymbol{r}) \to \Psi_n(\boldsymbol{r}) = \exp\left[\frac{ie}{\hbar}\chi(\boldsymbol{r})\tau_z'\right]\Phi_n(\boldsymbol{r}), \tag{B.1a}$$

$$\Delta(\boldsymbol{r}) \to \tilde{\Delta}(\boldsymbol{r}) = \exp\left[\frac{2ie}{\hbar}\chi(\boldsymbol{r})\right]\Delta(\boldsymbol{r}), \tag{B.1b}$$

under a gauge transformation $\boldsymbol{A} \to \tilde{\boldsymbol{A}} = \boldsymbol{A} + \nabla\chi(\boldsymbol{r})$. The transformation equations are such that they leave the BdG equations invariant for any differentiable function $\chi(\boldsymbol{r})$. The proof is only given for the bulk states but it is completely analogous for surface states. It follows the one given by de Gennes [4].

For the Hamiltonian to remain gauge invariant, we have to use canonical momentum operators $\boldsymbol{p} \to \boldsymbol{p} - e\boldsymbol{A}$. The BdG equations considered in eq. (3.3) become

$$\mathcal{H}(\boldsymbol{A})\Phi_n(\boldsymbol{r}) = E_n\Phi_n(\boldsymbol{r}), \tag{B.2a}$$

$$\begin{aligned}\mathcal{H}(\boldsymbol{A}) = \tau_z'\left(\frac{(\boldsymbol{p}-\tau_z'e\boldsymbol{A})^2}{2m^*} - \varepsilon_f\right) - \tau_z'\lambda_{so}(r)\left[\left(\boldsymbol{r}\times(\boldsymbol{p}-\tau_z'e\boldsymbol{A})\right)\cdot\boldsymbol{\sigma}'\right]_z \\ -m(r)\left[\boldsymbol{r}\times(\boldsymbol{p}-\tau_z'e\boldsymbol{A}) + \frac{\hbar}{2}\boldsymbol{\sigma}'\right]_z + \Delta(r)\exp\left[i\nu\theta\tau_z'\right]\tau_x'.\end{aligned} \tag{B.2b}$$

Before proceeding, consider this calculation.

$$\begin{aligned}\left(\boldsymbol{p}-\tau_z'e\tilde{\boldsymbol{A}}\right)\Psi_n(\boldsymbol{r}) &= \left(-i\hbar\nabla - \tau_z'e\tilde{\boldsymbol{A}}\right)\exp\left[\frac{ie}{\hbar}\chi(\boldsymbol{r})\tau_z'\right]\Phi_n(\boldsymbol{r}), \\ &= \exp\left[\frac{ie}{\hbar}\chi(\boldsymbol{r})\tau_z'\right]\left(-i\hbar\nabla + \tau_z'e\nabla\chi(\boldsymbol{r}) - \tau_z'e\tilde{\boldsymbol{A}}\right)\Phi_n(\boldsymbol{r}), \\ &= \exp\left[\frac{ie}{\hbar}\chi(\boldsymbol{r})\tau_z'\right]\left(\boldsymbol{p}-\tau_z'e\boldsymbol{A}\right)\Phi_n(\boldsymbol{r}).\end{aligned} \tag{B.3}$$

From this result, it follows that

$$\begin{aligned}\mathcal{H}(\tilde{\boldsymbol{A}})\Psi_n(\boldsymbol{r}) = &\left[\tau_z'\left(\frac{\left(\boldsymbol{p}-\tau_z'e\tilde{\boldsymbol{A}}\right)^2}{2m^*} - \varepsilon_f\right) - \tau_z'\lambda_{so}(r)\left[\left(\boldsymbol{r}\times(\boldsymbol{p}-\tau_z'e\tilde{\boldsymbol{A}})\right)\cdot\boldsymbol{\sigma}'\right]_z\right. \\ &\left.-m(r)\left[\boldsymbol{r}\times(\boldsymbol{p}-\tau_z'e\tilde{\boldsymbol{A}}) + \frac{\hbar}{2}\boldsymbol{\sigma}'\right]_z + \Delta(r)\exp\left[i\nu\theta\tau_z'\right]\exp\left[\frac{2ie}{\hbar}\chi(\boldsymbol{r})\tau_z'\right]\tau_x'\right]\Psi_n(\boldsymbol{r}), \\ = &\exp\left[\frac{ie}{\hbar}\chi(\boldsymbol{r})\tau_z'\right]\mathcal{H}(\boldsymbol{A})\Phi_n(\boldsymbol{r}).\end{aligned} \tag{B.4}$$

Here we have also used that $\tau_x'\exp\left[\frac{ie}{\hbar}\chi(\boldsymbol{r})\tau_z'\right] = \exp\left[-\frac{ie}{\hbar}\chi(\boldsymbol{r})\tau_z'\right]\tau_x'$. Multiplying eq. (B.2a) by $\exp\left[\frac{ie}{\hbar}\chi(\boldsymbol{r})\tau_z'\right]$, we find

$$\mathcal{H}(\tilde{\boldsymbol{A}})\Psi_n(\boldsymbol{r}) = E_n\Psi_n(\boldsymbol{r}), \tag{B.5}$$

in the new gauge. Thus, given a solution of the original equation (B.2a) (wave function $\Phi_n(\boldsymbol{r})$ with energies E_n), the transformed wave function $\Psi_n(\boldsymbol{r})$ will be a solution of the BdG equations in the new gauge. The energies remain unchanged, of course.

To cancel the phase of the pair potential $\Delta(\boldsymbol{r}) = \Delta(r)\exp[i\nu\theta]$, we choose $\chi(\boldsymbol{r}) = -\frac{\hbar}{2e}\nu\theta$ such that $\Psi_n(\boldsymbol{r}) = \exp\left[-i\frac{\nu}{2}\theta\tau_z\right]\Phi_n(\boldsymbol{r})$ and $\mathcal{H}(\tilde{\boldsymbol{A}}) = \tilde{\mathcal{H}}(\boldsymbol{r})$ in agreement with the unitary transformation in eq. (3.2). With this choice of $\chi(\boldsymbol{r})$, the transformed vector potential is given by

$$\tilde{\boldsymbol{A}} = \boldsymbol{A} - \frac{\hbar\nu}{2er}\hat{\boldsymbol{\theta}}. \tag{B.6}$$

C Rephrasing the BdG equations for the TSS

For the helical Dirac fermion TSS where $\hat{H}_N$ is given in eq. (2.5), $\tilde{\mathcal{H}}$ from the (gauge transformed) BdG equations (3.2) takes the form

$$\tilde{\mathcal{H}} = e^{-i\frac{\nu}{2}\theta\tau_z'} \left\{\tau_z' \left[v_D(\boldsymbol{\sigma'} \times \boldsymbol{p}) \cdot \hat{\boldsymbol{z}} - \varepsilon_f'\right] + \lambda_{so}'(r) L_z \sigma_z' \tau_z' - m'(r) J_z\right\} e^{i\frac{\nu}{2}\theta\tau_z'} + \Delta(r)\tau_x', \quad \text{(C.1)}$$

where we have used $-\sigma_y \boldsymbol{\sigma}^* \sigma_y = \boldsymbol{\sigma}$ and $\boldsymbol{p}^* = -\boldsymbol{p}$ to find $-\sigma_y (H_{kin}')^* \sigma_y = -H_{kin}'$ for the hole-like part. Note, however, that unlike the parabolic bulk band $\left[\tilde{\mathcal{H}}, L_z\right] \neq 0$ due to the changed kinetic part. The (2-D) total angular momentum operator $J_z = L_z + \frac{\hbar}{2}\sigma_z'$ does, however, commute with $\tilde{\mathcal{H}}$. We note that $\left[e^{-i\nu\theta\tau_z'/2} A e^{i\nu\theta\tau_z'/2}, J_z\right] = e^{-i\nu\theta\tau_z'/2}[A, J_z] e^{i\nu\theta\tau_z'/2}$ for all operators A and

$$\begin{aligned}\left[(\boldsymbol{\sigma'} \times \boldsymbol{p}) \cdot \hat{\boldsymbol{z}}, J_z\right] &= \left[\sigma_x' p_y - \sigma_y' p_x, L_z + \frac{\hbar}{2}\sigma_z'\right] \\ &= \sigma_x' \underbrace{\left[p_y, L_z\right]}_{i\hbar p_x} + \frac{\hbar}{2} \underbrace{\left[\sigma_x', \sigma_z'\right]}_{-2i\sigma_y'} p_y - \sigma_y' \underbrace{\left[p_x, L_z\right]}_{-i\hbar p_y} - \frac{\hbar}{2} \underbrace{\left[\sigma_y', \sigma_z'\right]}_{2i\sigma_x'} p_x = 0.\end{aligned} \quad \text{(C.2)}$$

Using these two results it should be fairly easy to show that $\left[\tilde{\mathcal{H}}, J_z\right] = 0$ such that we may find simultaneous eigenstates for the two operators.

$$\tilde{\mathcal{H}}\Psi_n(\boldsymbol{r}) = E_n \Psi_n(\boldsymbol{r}), \quad \text{(C.3a)}$$

$$J_z \Psi_n(\boldsymbol{r}) = \hbar\mu \Psi_n(\boldsymbol{r}). \quad \text{(C.3b)}$$

It's straightforward to verify that

$$\Psi_n(\boldsymbol{r}) = e^{i(\mu - \frac{1}{2}\sigma_z')\theta} \Psi_{n\mu}(r) \quad \text{(C.4)}$$

satisfies eq. (C.3b). We will use this slightly different partial wave expansion (compare with eq. (3.4)) for the TSS. Given the boundary condition $\Psi_n(r, \theta + 2\pi) = (-1)^\nu \Psi(r, \theta)$ from eq. (3.2), we write $\mu = l - \frac{\nu - 1}{2}$ where l is an integer. This means $\mu = \pm\frac{1}{2}, \pm\frac{3}{2}, ...$ is now a half-odd integer when the vorticity ν is even, and $\mu = 0, \pm 1, \pm 2, ...$ is an integer for odd ν which is opposite the bulk states.

In polar coordinates, we can write the kinetic part as

$$v_D(\boldsymbol{\sigma'} \times \boldsymbol{p}) \cdot \hat{\boldsymbol{z}} - \varepsilon_f' = i\hbar v_D \sigma_y' e^{i\theta\sigma_z'} \left(\partial_r + i\sigma_z' \frac{\partial_\theta}{r}\right) - \varepsilon_f'. \quad \text{(C.5)}$$

We insert the partial wave expansion (C.4) in the BdG equations (3.2) with $\tilde{\mathcal{H}}$ given in eq. (C.1) and cancel the phase terms to find the radial equation for the TSS.

$$\Bigg\{\tau_z'\left[i\hbar v_D\sigma_y'\left(\partial_r-\sigma_z'\frac{\mu-\frac{1}{2}\sigma_z'+\frac{\nu}{2}\tau_z'}{r}\right)-\varepsilon_f'\right]+\hbar\lambda_{so}'(r)\left(\mu-\frac{1}{2}\sigma_z'+\frac{\nu}{2}\tau_z'\right)\sigma_z'\tau_z' \\ -\hbar m'(r)\left[\left(\mu-\frac{1}{2}\sigma_z'+\frac{\nu}{2}\tau_z'\right)+\frac{1}{2}\sigma_z'\right]+\Delta(r)\tau_x'\Bigg\}\Psi_{n\mu}(r)=E_n^\mu\Psi_{n\mu}(r). \tag{C.6}$$

Similarly to the bulk states, we expand $\Psi_{n\mu}(r)$ in a set of Bessel functions. We choose the order of the Bessel functions to match the phase part $\exp\left[i(\mu-\frac{1}{2}\sigma_z'+\frac{\nu}{2}\tau_z')\right]$ of the full wave function $\Phi_n(\boldsymbol{r})$ in the old gauge, as before.

$$\Psi_{n\mu}(r)=\left[u_{n\mu_1^1\uparrow}(r),u_{n\mu_1^{-1}\downarrow}(r),v_{n\mu_{-1}^1\downarrow}(r),-v_{n\mu_{-1}^{-1}\uparrow}(r)\right]^T, \\ u_{n\mu_1^\sigma\sigma}(r)=\sum_{j=1}^J u_{n\mu_1^\sigma j\sigma}\phi_{\mu_1^\sigma j}(r),\qquad v_{n\mu_{-1}^\sigma\sigma}(r)=\sum_{j=1}^J v_{n\mu_{-1}^\sigma j\sigma}\phi_{\mu_{-1}^\sigma j}(r). \tag{C.7}$$

We have introduced a similar notation as in the case of the parabolic bulk band, namely $\mu_\tau^\sigma=\mu-\frac{1}{2}\sigma+\frac{\nu}{2}\tau$ with $\sigma,\tau=\pm1$ matching the entries in the four-component spinor $\Psi_{n\mu}(r)$. Analogously, we write

$$\Psi_{n\mu}(r)=\left[\Psi_{n\mu}^{11}(r),\Psi_{n\mu}^{-11}(r),\Psi_{n\mu}^{1-1}(r),\Psi_{n\mu}^{-1-1}(r)\right]^T, \tag{C.8a}$$

$$\Psi_{n\mu}^{\sigma\tau}(r)=\sum_{j=1}^J f_{n\mu j}^{\sigma\tau}\phi_{\mu_\tau^\sigma j}(r), \tag{C.8b}$$

$$f_{n\mu j}^{11}=u_{n\mu_1^1 j\uparrow},\ \ f_{n\mu j}^{-11}=u_{n\mu_1^{-1} j\downarrow},\ \ f_{n\mu j}^{1-1}=v_{n\mu_{-1}^1 j\downarrow},\ \ f_{n\mu j}^{-1-1}=-v_{n\mu_{-1}^{-1} j\uparrow}. \tag{C.8c}$$

Using this expansion, eq. (C.6) becomes

$$\sum_{j=1}^J\Bigg\{\left[-\tau\varepsilon_f'+\hbar\lambda_{so}'(r)\mu_\tau^\sigma\sigma\tau-\hbar m'(r)\left(\mu_\tau^\sigma+\frac{1}{2}\sigma\right)\right]f_{n\mu j}^{\sigma\tau}\phi_{\mu_\tau^\sigma j}(r) \\ +\tau\sigma\hbar v_D\left(\partial_r+\sigma\frac{\mu_\tau^{-\sigma}}{r}\right)f_{n\mu j}^{-\sigma\tau}\phi_{\mu_\tau^{-\sigma}j}(r)+\Delta(r)f_{n\mu j}^{\sigma-\tau}\phi_{\mu_{-\tau}^\sigma j}(r)\Bigg\}=\sum_{j=1}^J E_n^\mu f_{n\mu j}^{\sigma\tau}\phi_{\mu_\tau^\sigma j}(r). \tag{C.9}$$

We will need three Bessel function identities to simplify the kinetic part [9].

$$\int_a^b \mathrm{d}x\,xJ_l(\alpha x)J_l(\beta x)=\frac{1}{\alpha^2-\beta^2}\left[\beta xJ_l(\alpha x)J_l'(\beta x)-\alpha xJ_l(\beta x)J_l'(\alpha x)\right]_a^b, \tag{C.10a}$$

$$J_l'(x)\pm\frac{l}{x}J_l(x)=\pm J_{l\mp1}(x), \tag{C.10b}$$

$$J_{l-1}(x)+J_{l+1}(x)=\frac{2l}{x}J_l(x), \tag{C.10c}$$

where the prime denotes a derivative w.r.t. the variable x. When taking the inner product of eq. (C.9) with $\phi_{\mu^\sigma_\tau i}(r)$, the kinetic part presents us with the following integral (note $l' = l \pm 1$ in our case):

$$\begin{aligned}\int_0^R \mathrm{d}r\, r\phi_{li}(r)\left(\partial_r \pm \frac{l'}{r}\right)\phi_{l'j}(r) &\overset{\text{(C.10b)}}{=} \frac{\pm 2}{R^2 J_{l+1}(\beta_{li})J_{l'+1}(\beta_{l'j})}\frac{\beta_{l'j}}{R}\int_0^R \mathrm{d}r\, r J_l\left(\beta_{li}\frac{r}{R}\right)J_{l'\mp 1}\left(\beta_{l'j}\frac{r}{R}\right),\\ &\overset{\text{(C.10a)}}{=} \frac{\pm 2}{R^2 J_{l+1}(\beta_{li})J_{l'+1}(\beta_{l'j})}\frac{\beta_{l'j}}{R}\frac{R^2}{\beta_{li}^2-\beta_{l'j}^2}\left[-\beta_{li}J_l(\beta_{l'j})J_l'(\beta_{li})\right],\\ &\overset{\text{(C.10b)}}{=} \pm\frac{J_l(\beta_{l'j})}{J_{l'+1}(\beta_{l'j})}\frac{2}{R}\frac{\beta_{li}\beta_{l'j}}{\beta_{li}^2-\beta_{l'j}^2},\\ &\overset{\text{(C.10c)}}{=} -\frac{2}{R}\frac{\beta_{li}\beta_{l'j}}{\beta_{li}^2-\beta_{l'j}^2}.\end{aligned} \tag{C.11}$$

Taking the inner product of eq. (C.9) with $\phi_{\mu^\sigma_\tau i}(r)$ and using the above result, we write the radial equation as

$$\begin{aligned}\sum_{j=1}^{J}\Bigg\{&\left[-\tau\varepsilon_f'\delta_{ij} + \int_0^R \mathrm{d}r\, r\left(\hbar\lambda_{so}'(r)\mu^\sigma_\tau\sigma\tau - \hbar m'(r)\left(\mu^\sigma_\tau + \frac{1}{2}\sigma\right)\right)\phi_{\mu^\sigma_\tau i}(r)\phi_{\mu^\sigma_\tau j}(r)\right]f^{\sigma\tau}_{n\mu j}\\ &+\tau\sigma\left(\frac{-2\hbar v_D}{R}\frac{\beta_{\mu^\sigma_\tau i}\beta_{\mu^{-\sigma}_\tau j}}{\beta^2_{\mu^\sigma_\tau i}-\beta^2_{\mu^{-\sigma}_\tau j}}\right)f^{-\sigma\tau}_{n\mu j} + \left[\int_0^R \mathrm{d}r\, r\Delta(r)\phi_{\mu^\sigma_\tau i}(r)\phi_{\mu^\sigma_{-\tau} j}(r)\right]f^{\sigma-\tau}_{n\mu j}\Bigg\} = E^\mu_n f^{\sigma\tau}_{n\mu i}.\end{aligned} \tag{C.12}$$

We can simplify the notation if we introduce the matrix elements

$$(V_{\mu,\mu'})_{ij} = -\frac{2\hbar v_D}{R}\frac{\beta_{\mu i}\beta_{\mu' j}}{\beta^2_{\mu i}-\beta^2_{\mu' j}}, \tag{C.13a}$$

$$[(L_\mu)_{ij}, (M_\mu)_{ij}, (\Lambda_\mu)_{ij}] = \int_0^R \mathrm{d}r\, r\left[\mu\hbar m'(r), \frac{1}{2}\hbar m'(r), \mu\hbar\lambda_{so}'(r)\right]\phi_{\mu i}(r)\phi_{\mu j}(r), \tag{C.13b}$$

$$(\Delta_{\mu,\mu'})_{ij} = \int_0^R \mathrm{d}r\, r\Delta(r)\phi_{\mu i}(r)\phi_{\mu' j}(r). \tag{C.13c}$$

The radial equation then becomes

$$\begin{aligned}\sum_{j=1}^{J}\Big\{&\left[-\tau\varepsilon_f'\delta_{ij} + \sigma\tau(\Lambda_{\mu^\sigma_\tau})_{ij} - (L_{\mu^\sigma_\tau})_{ij} - \sigma(M_{\mu^\sigma_\tau})_{ij}\right]f^{\sigma\tau}_{n\mu j}\\ &+\tau\sigma(V_{\mu^\sigma_\tau,\mu^{-\sigma}_\tau})_{ij}f^{-\sigma\tau}_{n\mu j} + (\Delta_{\mu^\sigma_\tau,\mu^\sigma_{-\tau}})_{ij}f^{\sigma-\tau}_{n\mu j}\Big\} = E^\mu_n f^{\sigma\tau}_{n\mu i}.\end{aligned} \tag{C.14}$$

We may write this as a matrix eigenvalue problem similar to the parabolic bulk band.

$$\begin{pmatrix} -(L+M-\Lambda)_{\mu_1^1} - \varepsilon_f' & V_{\mu_1^1,\mu_1^{-1}} & \Delta_{\mu_1^1,\mu_{-1}^1} & 0 \\ V^T_{\mu_1^1,\mu_1^{-1}} & -(L-M+\Lambda)_{\mu_1^{-1}} - \varepsilon_f' & 0 & \Delta_{\mu_1^{-1},\mu_{-1}^{-1}} \\ \Delta^T_{\mu_1^1,\mu_{-1}^1} & 0 & -(L+M+\Lambda)_{\mu_{-1}^1} + \varepsilon_f' & -V_{\mu_{-1}^1,\mu_{-1}^{-1}} \\ 0 & \Delta^T_{\mu_1^{-1},\mu_{-1}^{-1}} & -V^T_{\mu_{-1}^1,\mu_{-1}^{-1}} & -(L-M-\Lambda)_{\mu_{-1}^{-1}} + \varepsilon_f' \end{pmatrix} \Psi_{n\mu} = E_n^\mu \Psi_{n\mu}, \tag{C.15}$$

where $\Psi_{nl} = [u_{\uparrow 1}, ..., u_{\uparrow J}, u_{\downarrow 1}, ..., u_{\downarrow J}, v_{\downarrow 1}, ..., v_{\downarrow J}, -v_{\uparrow 1}, ..., -v_{\uparrow J}]^T$ with suppressed indices n, μ_τ^σ. To solve the BdG equations, then, we diagonalize the matrix on the LHS numerically in the subspace of constant angular momentum μ.

D Symmetry of the basis functions

In this section we want to show that our normalized Bessel functions

$$\phi_{lj}(r) = \frac{\sqrt{2}}{RJ_{l+1}(\beta_{lj})} J_l\left(\beta_{lj}\frac{r}{R}\right), \qquad l \in \mathbb{Z},\ j \in \mathbb{N} \tag{D.1}$$

which we use as an orthonormal basis are in fact symmetric under inversion of angular momentum, i.e. $\phi_{lj}(r) = \phi_{-lj}(r)$.

For this we need two properties of the Bessel functions of the first kind of integer order l [9]:

$$J_{-l}(x) = (-1)^l J_l(x), \tag{D.2}$$

$$J_{l-1}(x) + J_{l+1}(x) = \frac{2l}{x} J_l(x). \tag{D.3}$$

The second property (D.3) actually applies to non-integer orders as well.

First note that the first property (D.2) implies that the roots of $J_{-l}(x)$ and $J_l(x)$ must be the same, i.e. $\beta_{-lj} = \beta_{lj}$. Then note that the second property (D.3) implies that

$$J_{l-1}(\beta_{lj}) = -J_{l+1}(\beta_{lj}) \tag{D.4}$$

since β_{lj} is a root of $J_l(x)$.

We now use these observations to rewrite $\phi_{-lj}(r)$.

$$\begin{aligned}\phi_{-lj}(r) &= \frac{\sqrt{2}}{RJ_{-l+1}(\beta_{-lj})} J_{-l}\left(\beta_{-lj}\frac{r}{R}\right) = \frac{\sqrt{2}}{R(-1)^{l-1}J_{l-1}(\beta_{lj})}(-1)^l J_l\left(\beta_{lj}\frac{r}{R}\right), \\ &= \frac{\sqrt{2}}{RJ_{l+1}(\beta_{lj})} J_l\left(\beta_{lj}\frac{r}{R}\right) = \phi_{lj}(r).\end{aligned} \tag{D.5}$$

This property will be used extensively in the numerical calculations to reduce (almost halve) computation time. Take a look at a generalized form of the integrals we need to compute in the A'th block of the Hamiltonian for fixed angular momentum l:

$$(A_l)_{ij} = f(l)\int_0^R \mathrm{d}r\, r w(r)\phi_{li}(r)\phi_{lj}(r), \tag{D.6}$$

where $f(l)$ and $w(r)$ are some weight functions (e.g. $f(l) = l$ and $w(r) = \Delta(r)$ or $w(r) = \exp[-r/r_0]$). Effectively, we only need to compute the Bessel functions and integrals for non-negative values of angular momentum.

E CdGM bound state wave functions and boundary effects

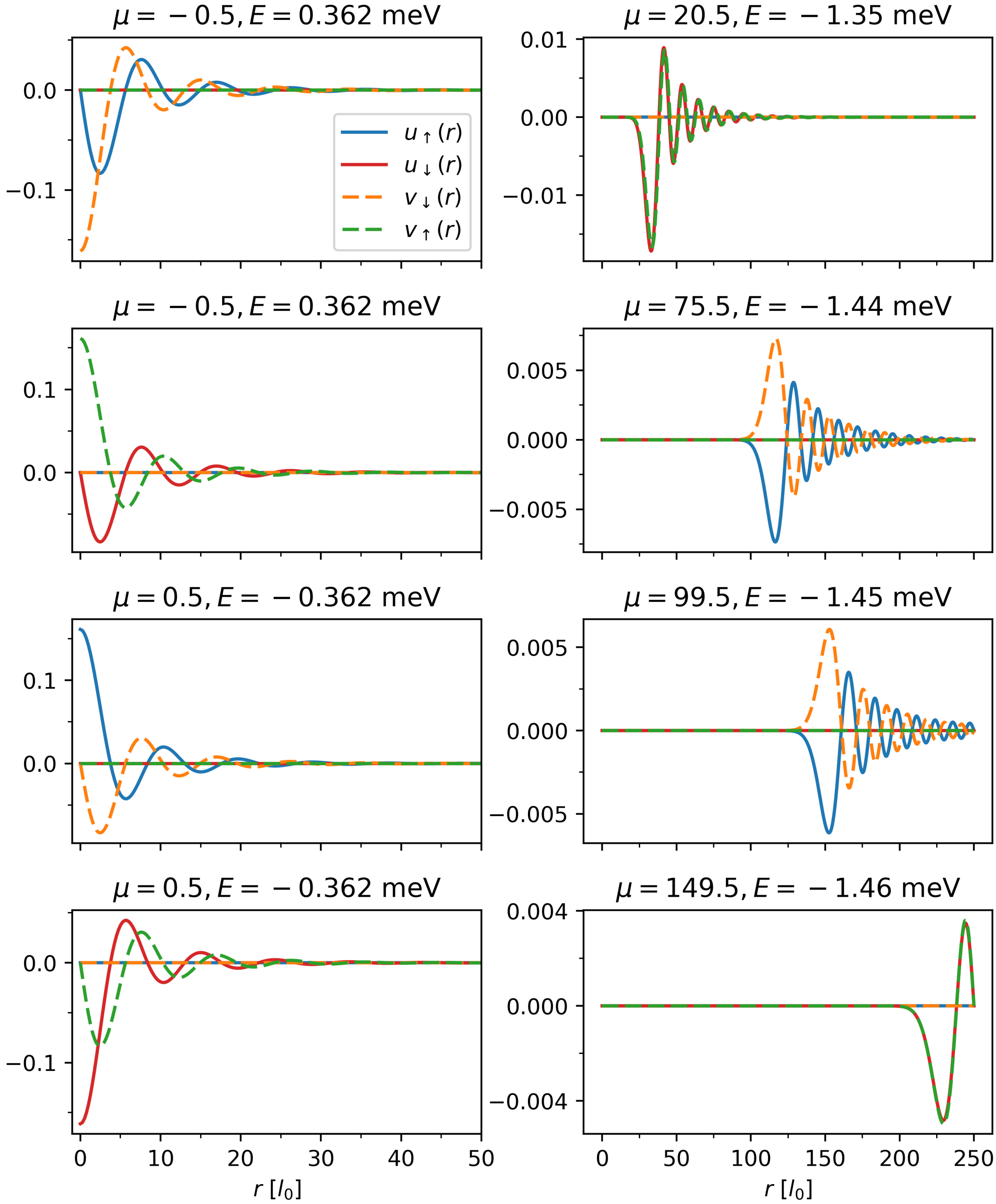

Figure E.1: Radial part of wave functions for some of the CdGM bound states shown in fig. 4.1(e). See upper left pane for legends.

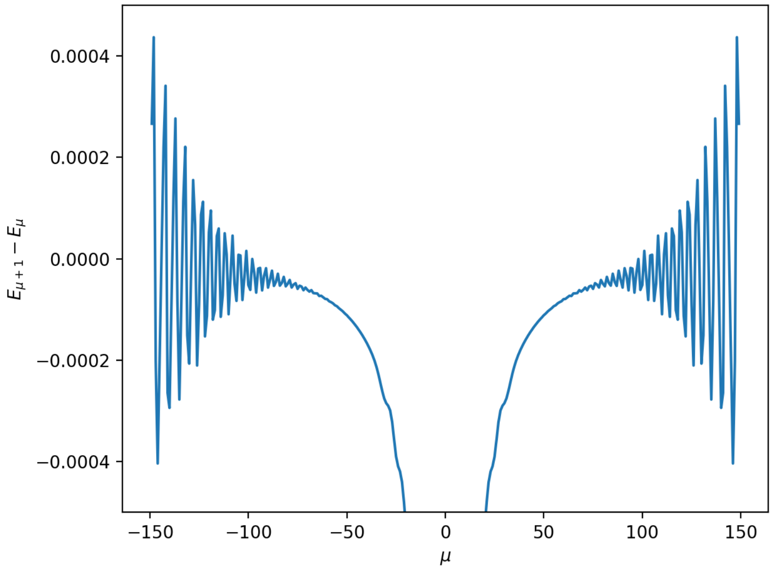

Figure E.2: Zoomed in view of the difference in energies between consecutive CdGM bound states showing the boundary effects on high angular momentum states. The differences is between the CdGM states shown in fig. 4.1(e).

F Extra figures for section 4.2

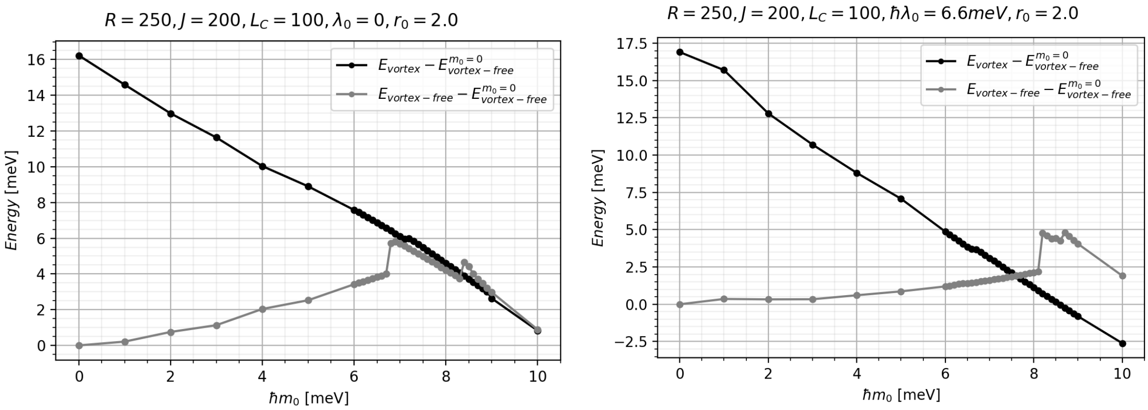

Figure F.1: Bulk layer with a single magnetic impurity. Energies of the vortex and vortex-free states measured from the energy of the vortex-free state with $m_0 = 0$ (LHS wo/ SOC; RHS w/ SOC). Vortex binding energy shown in fig. 4.2(c) is the difference of the two curves both with and without SOC. The decrease in binding energy for increased m_0 is primarily due to a lower energy vortex phase which decreases almost linearly (causing E_{vb} to do the same). The discontinuous jumps in the vortex-free energy happen when the YSR bound states cross the Fermi level since these are correlated with discontinuous jumps in the pairing profile (see appendix G). The energy of the vortex-free state increases in a simple manner until the bound states cross the Fermi level.

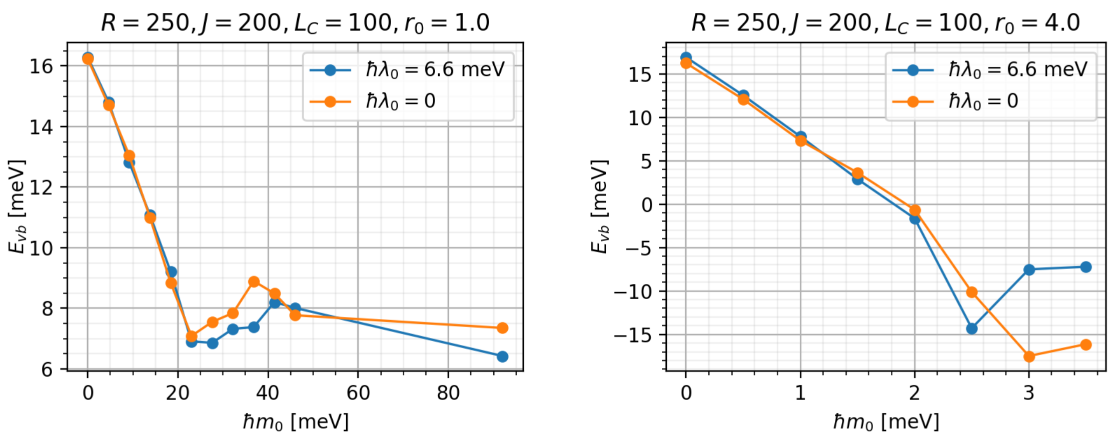

Figure F.2: Bulk layer with a single magnetic impurity. Vortex binding energy as function of exchange interaction strength for two different decay lengths. Vortex state is favored for $r_0 = 4$ both with and without SOC when $\hbar m_0 \gtrsim 2$ meV. Vortex state is never favored for $r_0 = 1$.

G Qualitative features of the vortex-free pairing profile

Here we discuss, very briefly, some of the preliminary observations of correlations between bound state Fermi level crossings and pair potential discontinuous jumps in the vortex-free case. Figure G.1 shows some of these jumps where the qualitative features of the pairing profile change substantially and discontinuously as in a first-order phase transition. There seems to be a correlation between Fermi level crossings of in-gap bound states and these discontinuous changes which also cause the total energy of the state to change discontinuously. This is evident from comparing figs. F.1, G.1, and G.2 with SOC; vortex-free YSR states cross the Fermi level at $\hbar m_0 = 8.1, 8.6$ meV. It's not quite clear whether these discontinuities are observed in the QAV-paper or if they are in a different parameter regime where no Fermi level crossings occur for the YSR states in the vortex-free state.

Before the first Fermi level crossing $0 < m_0 \leq m_0^c{}'$, the pairing profile shows a broad suppression by the presence of the impurity. The first crossing seems to give rise to a large dip in the pairing profile near the core. It's observed as a seemingly general feature that the pairing profile switches sign discontinuously when the $l = 0$ YSR states cross the Fermi level. This is the tuning value, denoted $m_0^c{}''$, used for the YSR ZBS in the parabolic bulk band discussed in section 4.5. The sign-switching is shown, perhaps more clearly, in fig. G.3. The same sign-switching qualitative behavior is also found by Flatté and Byers [17].

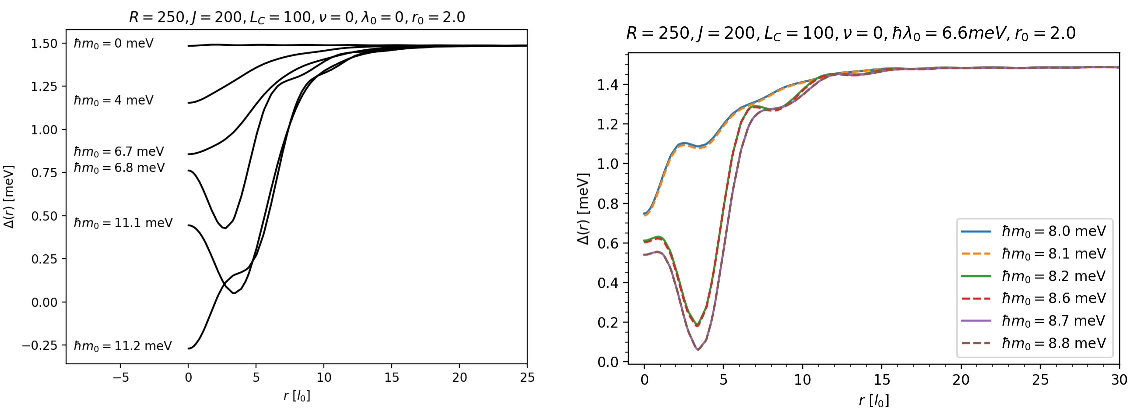

Figure G.1: Self-consistent pairing profiles for different exchange interaction strengths in the vortex-free case with $r_0 = 2$ showing discontinuous jumps. Left side: no SOC ($\lambda_0 = 0$) and $\hbar m_0^c{}' \simeq 6.7$ meV, $\hbar m_0^c{}'' \simeq 11.1$ meV; right side: SOC ($\hbar\lambda_0 = 6.6$ meV) and $\hbar m_0^c{}' \simeq 8.1$ meV ($\hbar m_0^c{}''$ above parameter range).

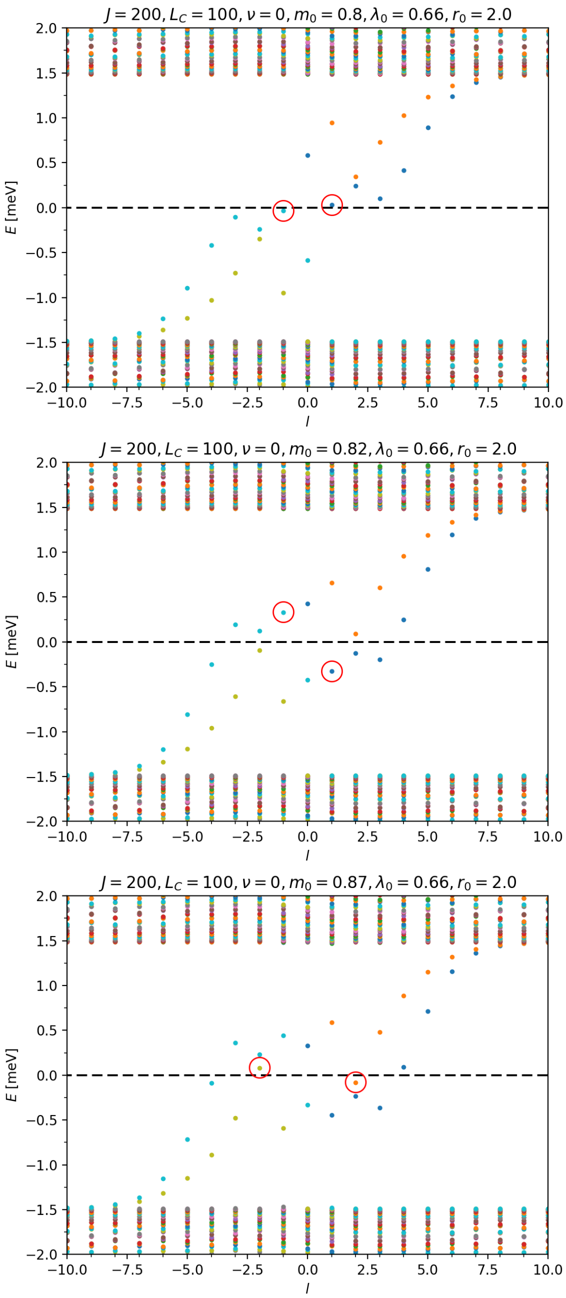

Figure G.2: Energy level spectra showing YSR state Fermi level crossings and discontinuous jumps in energies – with SOC ($\hbar\lambda_0 = 6.6$ meV). These should be compared with the RHS of fig. G.1. Crossings occur between $\hbar m_0 = 8.1, 8.2$ meV and between $\hbar m_0 = 8.6, 8.7$ meV. Fermi level is marked with a dashed line and the crossing states are outlined with a red circle. Units in titles are 10 meV/$\hbar$ for m_0, λ_0.

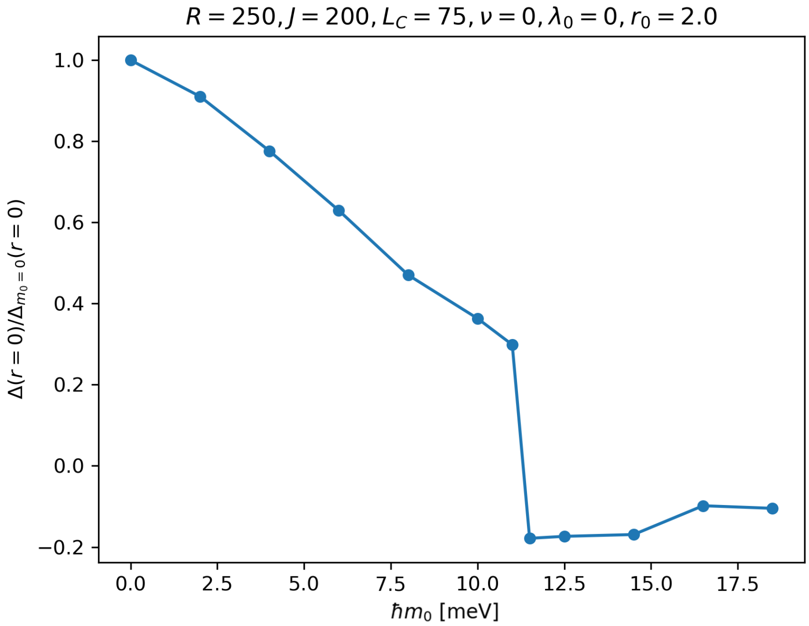

Figure G.3: Self-consistent pairing profile evaluated at impurity for different exchange interaction strengths in the vortex-free case without SOC. The discontinuity at $\hbar m_0^{c\prime\prime} \simeq 11.1$ meV from the LHS of fig. G.1 is clearly visible.

H (Anti-)ferromagnetic exchange interactions

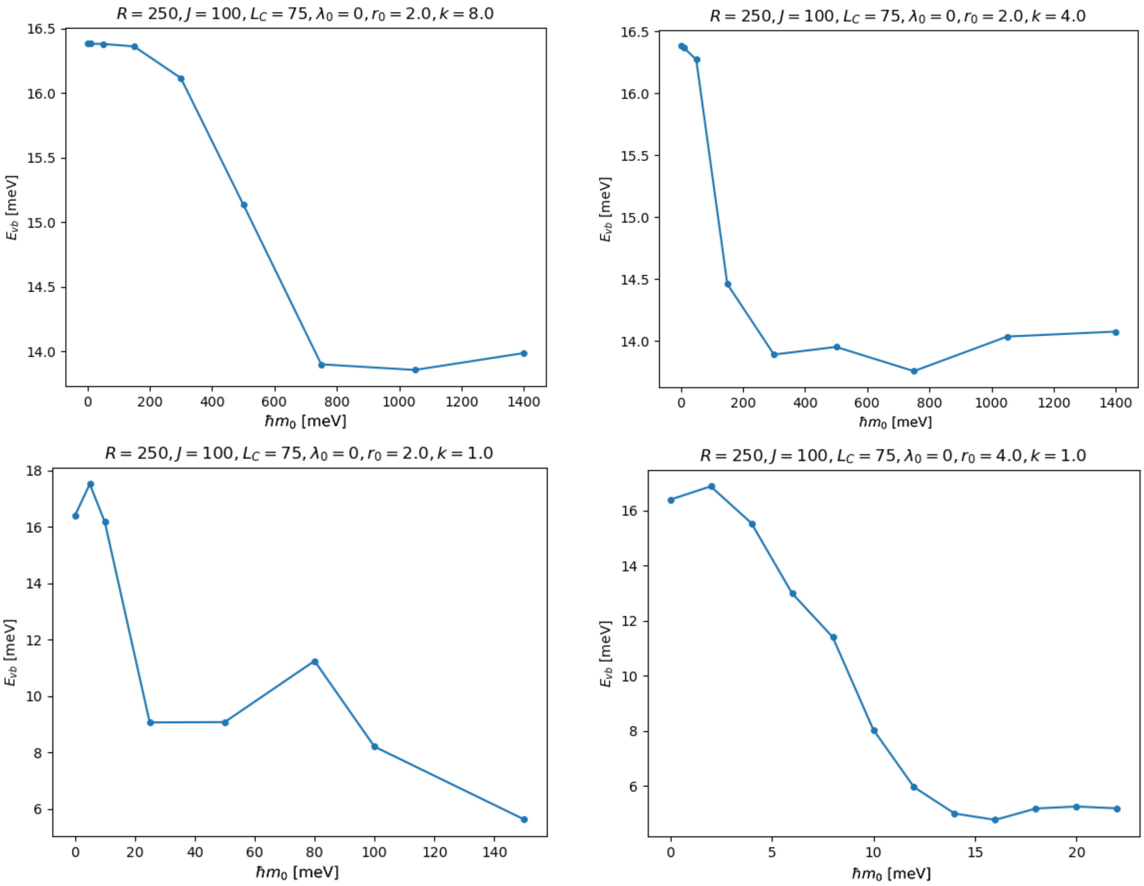

Figure H.1: Vortex binding energy as function of the exchange interaction strength m_0 for the anti-ferromagnetic exchange interaction $m(r) = m_0 \cos(kr)e^{-r/r_0}$ discussed in section 4.3 for different parameters r_0, k without SOC. The vortex state is never favored even in the case $r_0 = 4, k = 1$ which is most similar to the simple exponential decay $m(r) = m_0 e^{-r/r_0}$ of the single magnetic impurity discussed in section 4.2.

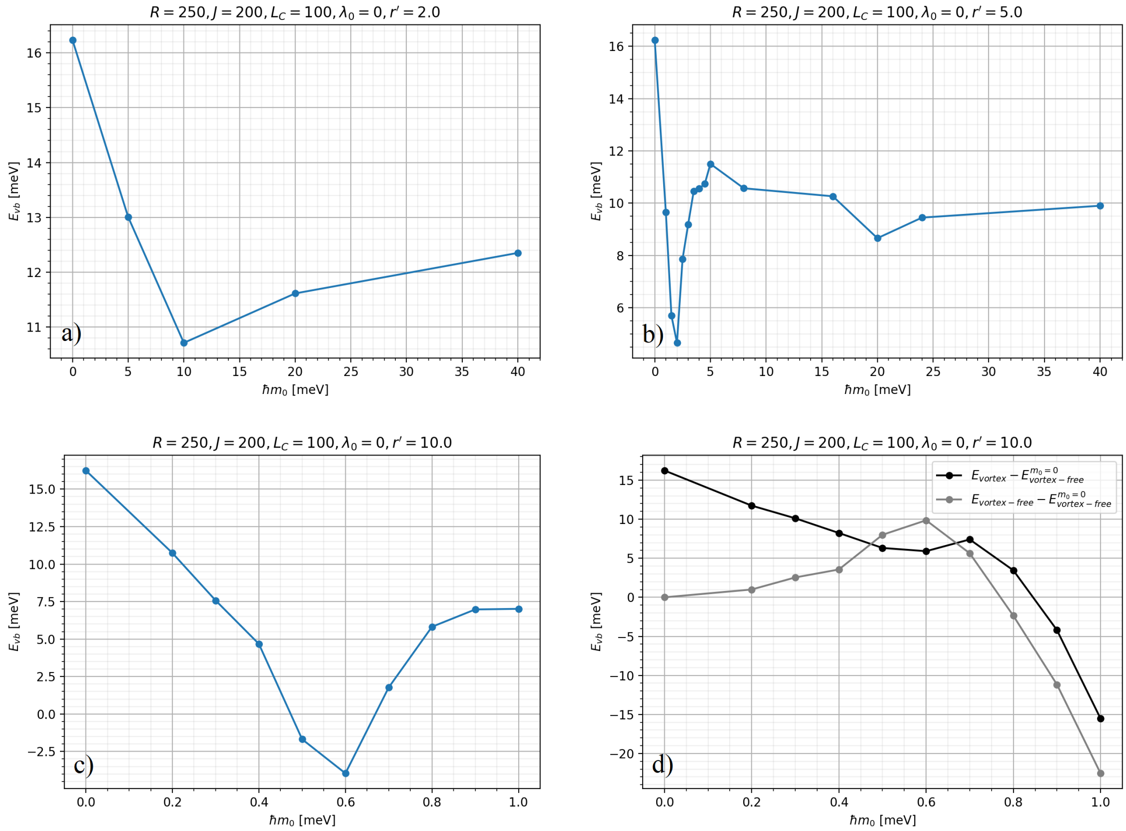

Figure H.2: Energy calculations for the extended ferromagnetic exchange interaction $m(r) = m_0 \frac{1}{2}\left(1 - \tanh\left(\frac{r-r'}{0.4 l_0}\right)\right)$ discussed in section 4.3 for different parameters r' without SOC. (a-c) Vortex binding energy as function of the exchange interaction strength m_0 for radius $r' = 2, 5, 10$. (d) Energy of the vortex and vortex-free states measured from the vortex-free energy of the $m_0 = 0$ case for radius $r' = 10$. The vortex state is favored for $r' = 10$ in the range 0.5 meV $\lesssim \hbar m_0 \lesssim$ 0.7 meV but not for the two other radii.

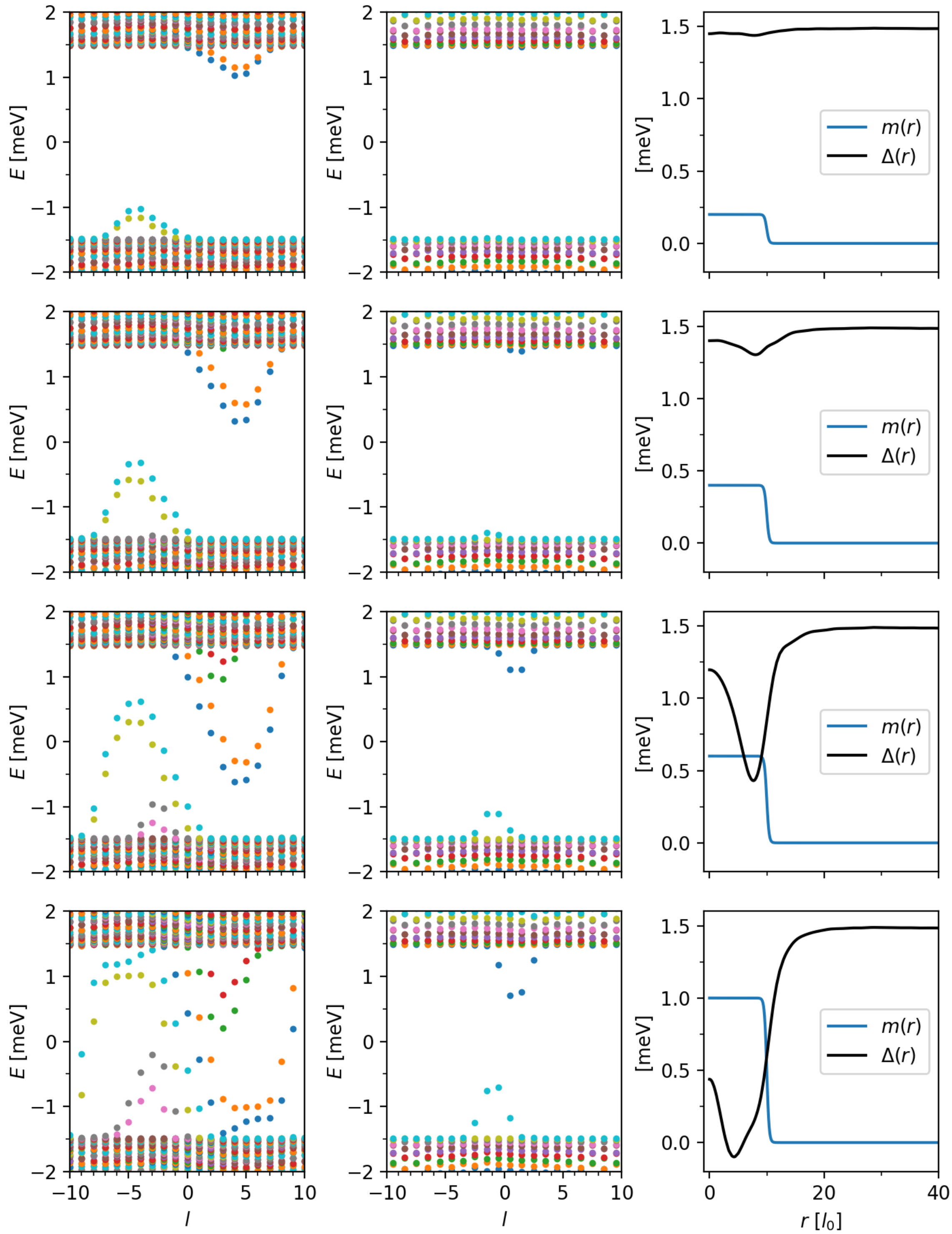

Figure H.3: Energy spectra, self-consistent pairing profiles, and exchange coupling profiles for the *vortex-free* state with extended ferromagnetic exchange interaction $m(r) = m_0 \frac{1}{2}\left(1 - \tanh\left(\frac{r-r'}{0.4 l_0}\right)\right)$ and $r' = 10$ for different interaction strengths. The plots are matched row-wise with $\hbar m_0 = 0.2,\ 0.4,\ 0.6,\ 1.0$ meV for row 1,2,3,4, respectively. Column 1,2 are energy spectra for the hole-like parabolic bulk band and helical Dirac fermion TSS, respectively. Column 3 shows the self-consistent pairing profiles and exchange couplings used to generate the energy spectra.

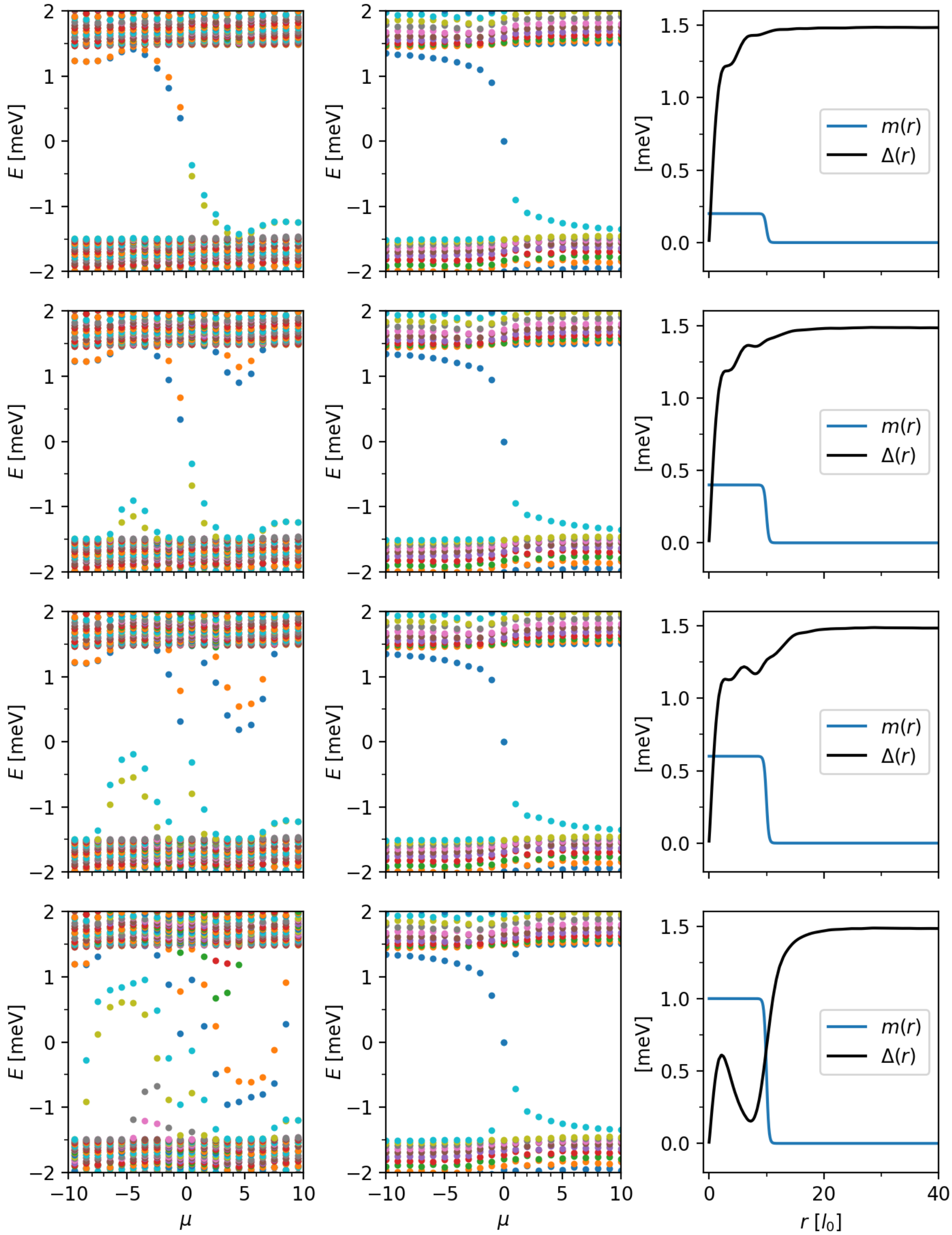

Figure H.4: Energy spectra, self-consistent pairing profiles, and exchange coupling profiles for the *vortex* state with extended ferromagnetic exchange interaction $m(r) = m_0 \frac{1}{2}\left(1 - \tanh\left(\frac{r-r'}{0.4l_0}\right)\right)$ and $r' = 10$ for different interaction strengths. The plots are matched row-wise with $\hbar m_0 = 0.2,\ 0.4,\ 0.6,\ 1.0$ meV for row 1,2,3,4, respectively. Column 1,2 are energy spectra for the hole-like parabolic bulk band and helical Dirac fermion TSS, respectively. Column 3 shows the self-consistent pairing profiles and exchange couplings used to generate the energy spectra.

I Surface layer ZBS wave functions

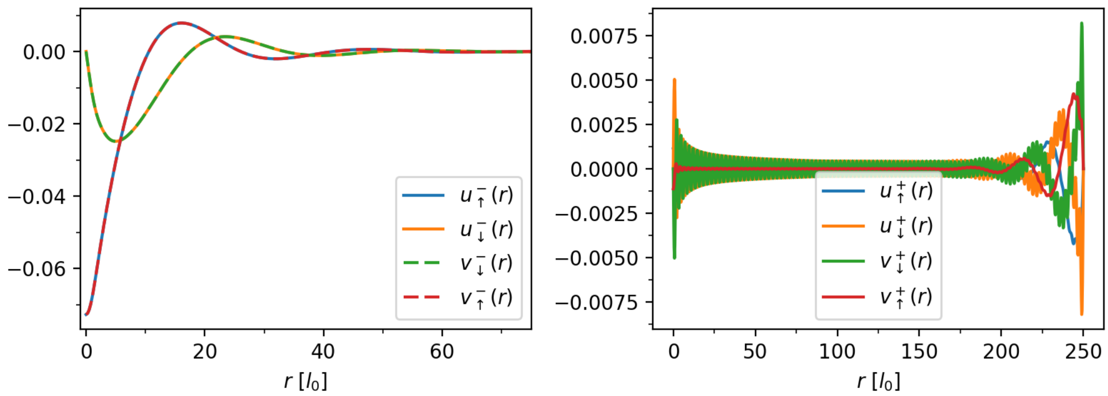

Figure I.1: Wave functions for the linear combinations of the ZBSs discussed in section 4.4. Left (right) pane is the radial part of the wave function for $\Psi^{-}(\boldsymbol{r})$ $(\Psi^{+}(\boldsymbol{r}))$.

J Zeeman splitting of zero-energy bound states

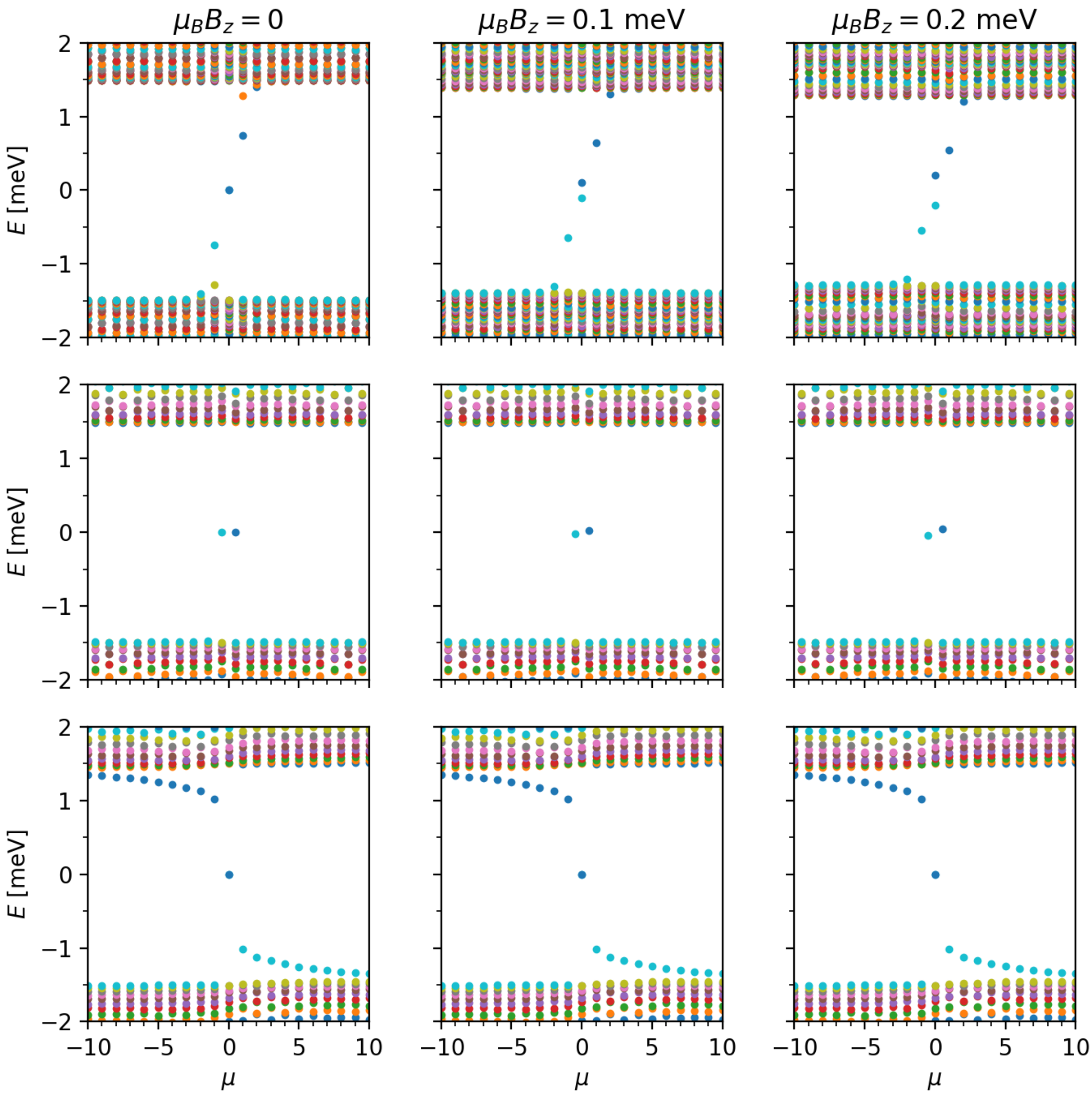

Figure J.1: Perturbative Zeeman effect. Energy spectra for the tuned YSR ZBSs in both the parabolic bulk band (first row) and TSS (second row) compared to the Majorana mode of the QAV-coupled TSS (third row) for different impurity-aligned external magnetic field strengths. Both the bulk and surface YSR ZBSs show Zeeman splitting whereas the two ZBSs in the TSS stay fixed at zero energy. The exchange interaction tuning values are $\hbar m_0 = 61.7$ meV and $\hbar m_0 = 229$ meV for the parabolic bulk band and TSS, respectively.

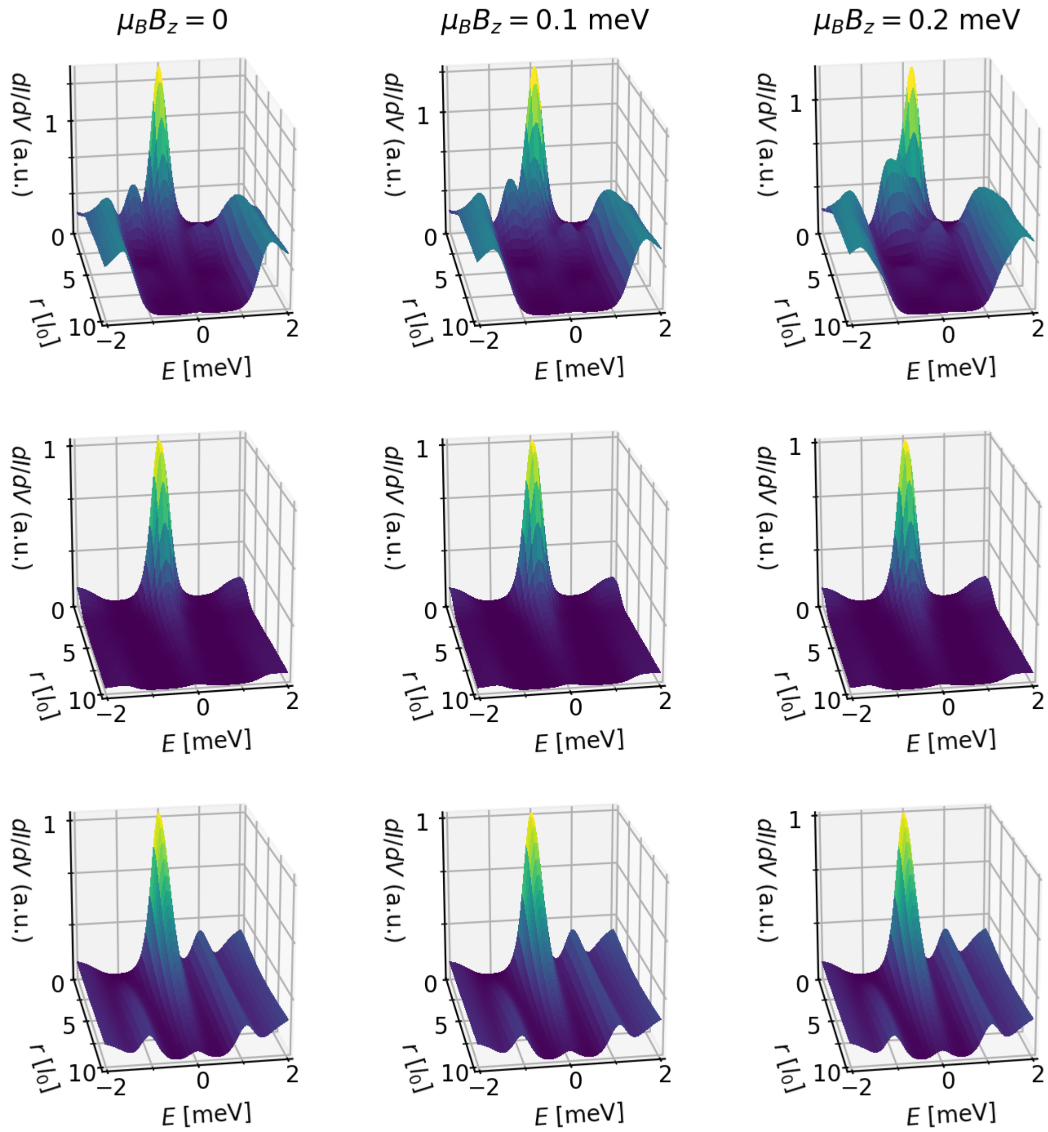

Figure J.2: Perturbative Zeeman effect. LDOS corresponding to the energy spectra of fig. J.1. It's difficult to see in the figure, but the vortex-free TSS zero-bias peak shifts upward in bias energy; the Majorana mode stays fixed.

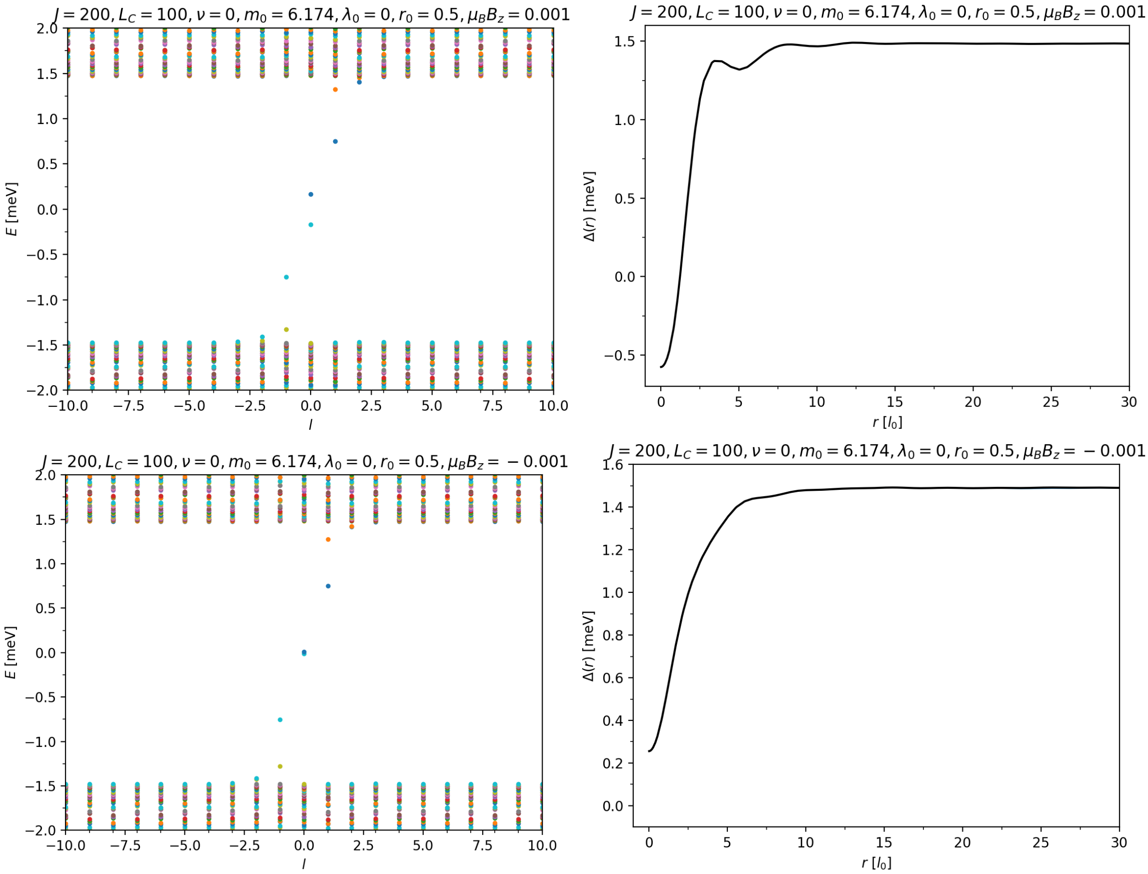

Figure J.3: Self-consistent Zeeman effect of tuned YSR ZBSs in the parabolic bulk band with $\mu_B B_z = 0.01$ meV. The top row shows a magnetic field aligned parallel with the magnetic moment of the impurity, changing the pairing profile significantly which leads to a discontinuous jump in the energy splitting of the before ZBSs. The bottom row shows a magnetic field of the same strength anti-aligned with the moment of impurity and a considerably smaller Zeeman splitting consistent with a perturbative calculation. Note that the magnetic field $\mu_B B_z = 0.01$ meV is much smaller than in fig. J.1 and J.2.

Bibliography

[1] J. X. Yin et al., *Observation of a robust zero-energy bound state in iron-based superconductor Fe(Te,Se)*, Nat. Phys. **11**, 543 (2015).

[2] K. Jiang, X. Dai, and Z. Wang, *Quantum Anomalous Vortex and Majorana Zero Mode in Iron-Based Superconductor Fe(Te,Se)*, Phys. Rev. X **9**, 011033 (2019).

[3] H. Deng, N. Bonesteel, and P. Schlottmann, *Bound fermion states in pinned vortices in the surface states of a superconducting topological insulator*, Journal of Physics: Condensed Matter **33**, 035604 (2020).

[4] P. G. de Gennes, *Superconductivity of Metals and Alloys* (CRC Press, 2018 (1966)).

[5] J. Sólyom, *Fundamentals of the Physics of Solids, Volume 3 - Normal, Broken-Symmetry, and Correlated Systems* (Springer-Verlag Berlin Heidelberg, 2010).

[6] J. F. Annett, *Superconductivity, superfluids, and condensates* (Oxford University Press, 2004).

[7] H. Sura, *Note on reformulating the BdG equations*, May 2021.

[8] K. Jiang, X. Dai, and Z. Wang, *Supplemental material for Quantum anomalous vortex and Majorana zero mode in iron-based superconductor Fe(Te,Se)*, Feb. 2019.

[9] K. F. Riley and M. P. Hobson, *Essential mathematical methods for the physical sciences* (Cambridge University Press, 2011).

[10] C. Caroli, P. G. de Gennes, and J. Matricon, *Bound fermion states on a vortex line in a type II superconductor*, Phys. Lett. **9**, 307 (1964).

[11] H. F. Hess, R. B. Robinson, and J. V. Waszczak, *Vortex-core structure observed with a scanning tunneling microscope*, Phys. Rev. Lett. **64**, 2711 (1990).

[12] F. Gygi and M. Schlüter, *Self-consistent electronic structure of a vortex line in a type-II superconductor*, Phys. Rev. B **43**, 7609 (1991).

[13] L. Yu, *Bound state in superconductors with paramagnetic impurities*, Acta Phys. Sin. **21**, 75 (1965).

[14] H. Shiba, *Classical spins in superconductors*, Prog. Theor. Phys. **40**, 435 (1968).

[15] A. I. Rusinov, *Superconductivity near a paramagnetic impurity*, JETP Lett. **9**, 85 (1969).

[16] V. Thampy et al., *Friedel-Like Oscillations from Interstitial Iron in Superconducting* $Fe_{1+y}Te_{0.62}Se_{0.38}$, Phys. Rev. Lett. **108**, 107002 (2012).

[17] M. E. Flatté and J. M. Byers, *Local electronic structure of defects in superconductors*, Phys. Rev. B **56**, 11213 (1997).